

## EFFICIENT 2D AND 3D SHOT RECORD REDATUMING<sup>1</sup>

N. A. KINNEGING<sup>2</sup>, V. BUDEJICKY<sup>3</sup>,  
C. P. A. WAPENAAR<sup>2</sup> and A. J. BERKHOUT<sup>2</sup>

### ABSTRACT

KINNEGING, N.A., BUDEJICKY, V., WAPENAAR, C.P.A. and BERKHOUT, A.J. 1989. Efficient 2D and 3D shot record redatuming. *Geophysical Prospecting* 37, 493–530.

In order to make 3D prestack depth migration feasible on modern computers it is necessary to use a target-oriented migration scheme. By limiting the output of the migration to a specific depth interval (target zone), the efficiency of the scheme is improved considerably. The first step in such a target-oriented approach is redatuming of the shot records at the surface to the upper boundary of the target zone. For this purpose, efficient non-recursive wavefield extrapolation operators should be generated. We propose a ray tracing method or the Gaussian beam method. With both methods operators can be efficiently generated for any irregular shooting geometry at the surface. As expected, the amplitude behaviour of the Gaussian beam method is better than that of the ray tracing based operators.

The redatuming algorithm is performed per shot record, which makes the data handling very efficient. From the shot records at the surface 'genuine zero-offset data' are generated at the upper boundary of the target zone. Particularly in situations with a complicated overburden, the quality of target-oriented zero-offset data is much better than can be reached with a CMP stacking method at the surface. The target-oriented zero-offset data can be used as input to a full 3D zero-offset depth migration scheme, in order to obtain a depth section of the target zone.

### INTRODUCTION

During the last decade the seismic industry has gradually been shifting from 2D data acquisition and processing to 3D techniques. The main causes of this important shift are: (i) The Earth is 3D and a 2D description is therefore incorrect. For strongly inhomogeneous subsurfaces the 2D assumption breaks down completely.

<sup>1</sup> Based on a paper read at the 50th EAEG meeting, The Hague; revision accepted January 1989.

<sup>2</sup> Delft University of Technology, Laboratory of Seismics and Acoustics, P.O. Box 5046, 2600 GA Delft, The Netherlands.

<sup>3</sup> Delft University of Technology. Present address: Jason Geosystems B.V., P.O. Box 596, 2600 AN Delft, The Netherlands.

Out-of-plane events and amplitudes are handled incorrectly. (ii) The development of electronics and computers in the last decade has made it possible to do 3D acquisition and processing in an economically justifiable way. The shift from 2D to 3D imposes heavy constraints on the acquisition and demands large and fast computers. Until the arrival of large supercomputers, it was difficult to do 3D processing in practice.

Despite the increase in the possibilities of supercomputers, it is still not feasible to perform a full 3D prestack depth migration. Current 3D processing still consists of conventional CMP stacking followed by post-stack migration. It is well known that CMP stacking may distort the data considerably, especially where there are strong lateral velocity variations. This means that a lot of the advantages of 3D processing are diminished by the stacking process. It is therefore important to develop a method that does not have the problems of conventional CMP stacking but that is also efficient such that stacking can be performed within a reasonable CPU time on modern supercomputers. One way to improve the quality of the processing is by improving the stacking technique and therefore much work has been done in developing DMO techniques. However, DMO is designed for constant velocity media. For strongly inhomogeneous media DMO may even diminish the quality of the data. Therefore we propose a full prestack approach to 3D data processing. In this paper we pay special attention to an efficient implementation.

The basic principle to develop such an efficient scheme is to separate the subsurface of the earth into two parts, namely a target zone and an overburden. After conventional processing the geologist indicates a part of the subsurface, the target zone, in which he is especially interested. With the proposed scheme, a high quality detailed reflectivity image is calculated only for this part of the subsurface. This is the so-called target-oriented approach to 3D prestack migration (TRITON, 1985).

The target-oriented scheme consists of a number of separate steps:

(1) *Surface related pre-processing.* Here the surface related multiples are eliminated. After this step the reflecting surface is effectively replaced by a reflection-free surface and the data can be considered as the upgoing part of the pressure field. More information can be found in Verschuur *et al.* (1988).

(2) *Estimation of the macro-subsurface model.* This model contains the main geological boundaries and interval velocities. It describes the propagation of the seismic waves through the overburden. The best known method for the macro-model estimation is Dix's formula (1955) and the extensions made by Hubral (1976). Van der Made (1988) gave an alternative method for this estimation.

(3) *Redatuming of the shot records at the surface to the upper boundary of the target zone.* In this step the surface data is extrapolated to the target upper boundary and there 'genuine' zero-offset data is generated. The distorting propagation effects of the overburden are eliminated in this step. Prestack 2D redatuming was described by Berryhill (1984) and Peels (1988).

(4) *Verification of the macro-subsurface model.* After redatuming the macro-subsurface model used is checked for correctness by means of a focusing analysis. For minor errors in the macro-model used the data can be corrected by applying a residual NMO correction. For larger errors the macro-model has to be updated and

a new redatuming must be performed. This verification and updating method was described by Jeannot, Faye and Denelle (1986) and Cox *et al.* (1988).

(5) *Zero-offset depth migration within the target zone.* Finally the zero-offset output data of the redatuming is migrated by a one-pass depth algorithm. It results in a detailed depth section of the target zone. This scheme can be efficiently implemented by storing the operators in a table (Holberg 1987; Blacqui re *et al.* 1989). In some cases the velocity structure within the target zone is relatively simple, such that no full depth migration is necessary. Yilmaz and Lucas (1986) showed an example where, after elimination of the effect of the sea bottom topography, a time migration algorithm could be used. However a post-stack *depth* migration scheme will recover a high quality depth section of the target zone without the simplifying assumptions of a *time* migration scheme.

Because no detailed reflectivity of the overburden is aimed at, this scheme is much more efficient than full 3D prestack migration. It makes the scheme feasible on modern (super)computers. The conventional CMP stacking is avoided. Due to the full 3D redatuming of the shot records, combined with a full 3D migration scheme, an image of the target zone can be obtained that is much better than can be obtained by conventional CMP stacking and post-stack migration.

We will focus on the second step in this scheme, the 3D redatuming. Schultz and Sherwood (1980) have already mentioned the possibility of redatuming to a certain level and doing a post-stack processing below that level in their paper on 2D prestack depth migration. Berryhill (1984, 1986) described the conventional implementation of redatuming in three steps: (i) downward extrapolation of the receivers to the new datum, (ii) reordering the data from common shot gathers to common receiver gathers, and (iii) downward extrapolation of the sources to the new datum, using the reciprocity property.

The result of this redatuming scheme is a prestack data set as if it had been measured at the new datum. There is an obvious reason why this scheme is not well suited for 3D applications. In 2D applications the reordering of the data can be avoided: on most of the modern computers a full monochromatic data set can easily be kept in core. However, in 3D this reordering cannot be circumvented. Due to the huge amount of data, a lot of I/O is required, which causes serious problems.

We describe a 3D shot record redatuming scheme. By redatuming per shot record, the reordering of the data into common receiver gathers is avoided. Furthermore, the amount of data to be kept in core at any time is limited. Therefore the problems that conventional redatuming schemes would encounter in 3D are avoided here, while the quality of the result stays exactly the same. This important advantage of the shot record approach is not always fully appreciated (see e.g. Jeannot 1988).

As can be deduced from the above, wavefield extrapolation plays a key role in redatuming. It is very important to develop an efficient method for extrapolation. We use both ray tracing as well as the Gaussian beam method to calculate non-recursive extrapolation operators. We thus obtain in an efficient way operators that are valid for strongly lateral and vertical inhomogeneous media. The concept of using ray tracing for the calculation of extrapolation operators is also employed by

Beydoun and Kebo (1987) and Kebo and Beydoun (1988) in a time-domain implementation of a Kirchhoff migration scheme.

The scheme described here is constructed in such a way that the results can be easily used from any available ray tracing package. The actual redatuming is applied per monochromatic component, as is done with all our migration related techniques. Both for 2D as well as for 3D different ray tracing packages are commercially available.

In comparison with ray tracing, the Gaussian beam method has several important advantages: (i) it has a better amplitude behaviour than ray tracing, (ii) it is stable in case of caustics, and (iii) shadow zones, that frequently occur in ray tracing methods, are avoided.

Besides these advantages the Gaussian beam algorithm is, just like ray tracing, very efficient. Wapenaar *et al.* (1989) introduce the use of Gaussian beams for the development of inverse wavefield extrapolation operators.

Our paper can be subdivided into two main parts. In the first part the theory and the implementation of inverse wavefield extrapolation are discussed. In the second part the application to shot record redatuming is shown.

The first part reviews the general theory of wavefield extrapolation. Then special attention is paid to the Gaussian beams. The principle of Gaussian beams is discussed with a simple modelling example and the main results from the theory are presented. After the introduction of Gaussian beams we discuss how both the ray tracing as well as the Gaussian beam method can be implemented in a scheme for inverse wavefield extrapolation. A comparison between the two methods is made for the inverse extrapolation of a 2D wavefield. Also the inverse extrapolation of a 3D wavefield through an inhomogeneous subsurface are demonstrated.

The second part discusses the theory of shot record redatuming. It is shown that the results of shot record redatuming are identical to the results of so-called 'full' prestack redatuming. Finally the results of redatuming of 2D and 3D prestack data are presented.

## WAVEFIELD EXTRAPOLATION

Wavefield extrapolation plays a key role in the redatuming scheme. Berkhout and Wapenaar (1989) and Wapenaar *et al.* (1989) describe the theory of both forward and inverse one-way extrapolation through complex media.

A thorough description of wavefield extrapolation is beyond the scope of this paper, but the main results are discussed here. Consider the geometry as depicted in Fig. 1. The upgoing (reflected) wavefield at  $z = z_A$  must be calculated from the wavefield at  $z = z_0$ . The closed surface Kirchhoff integral over  $S_0$ ,  $S_1$  and  $S_2$  can be approximated by a surface integral over acquisition surface  $S_0$  only (as shown by Wapenaar *et al.* 1989):

$$P^-(\mathbf{r}_A, \omega) = - \int_{S_0} \left[ \nabla G^* \frac{1}{\rho} P - G^* \frac{1}{\rho} \nabla P \right] \cdot \mathbf{n} \, dS_0, \quad (1)$$

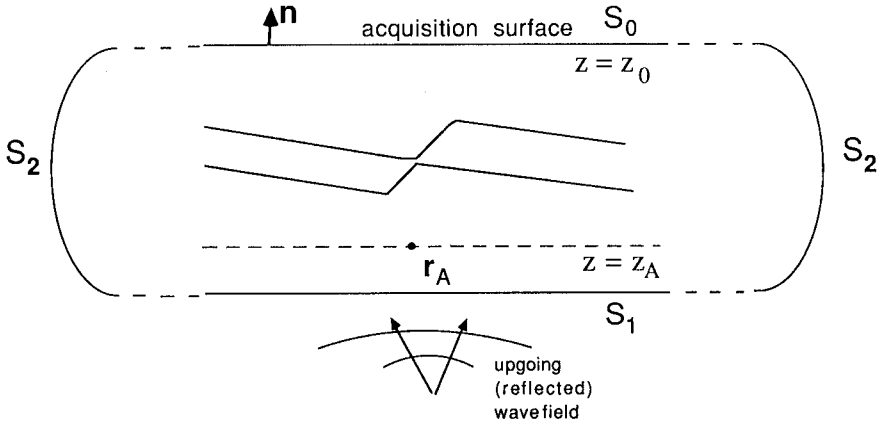


FIG. 1. Geometry for inverse extrapolation from  $z_0$  to  $z_A$ .

where  $P = P(\mathbf{r}, \omega)$  is the acoustic pressure,  $P^-(\mathbf{r}_A, \omega)$  is the upgoing component of the extrapolated pressure wavefield at  $\mathbf{r} = \mathbf{r}_A$ ,  $G = G(\mathbf{r}, \mathbf{r}_A, \omega)$  is the Green's wavefield at  $\mathbf{r}$  for a Green's point source located at  $\mathbf{r}_A$  (see Fig. 2 for a schematic representation of this Green's function),  $G^* = G^*(\mathbf{r}, \mathbf{r}_A, \omega)$  is the backpropagating Green's wavefield (the symbol \* denotes the complex conjugate), and  $\rho$  is the mass density.

In (1) the following approximations are made: (i) evanescent waves are neglected, which is common practice in seismic processing and (ii) Second-order amplitude effects such as internal multiples are neglected, which is normal for the one-way approximation.

This Kirchhoff integral can be further simplified to a Rayleigh integral, when  $S_0$

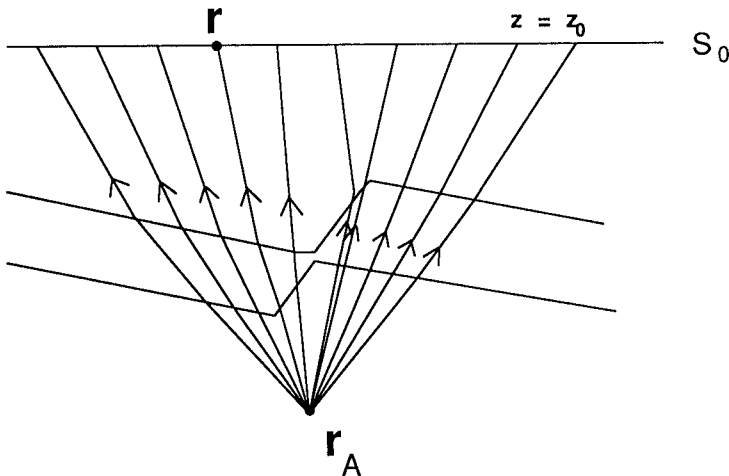


FIG. 2. Schematic representation of the Green's wavefield  $G(\mathbf{r}, \mathbf{r}_A, \omega)$ .

is a plane surface at  $z = z_0$  :

$$P^-(\mathbf{r}_A, \omega) = 2 \int_{-\infty}^{\infty} \int_{-\infty}^{\infty} \left[ \left( \frac{\partial G^-(\mathbf{r}, \mathbf{r}_A, \omega)}{\partial z} \right)^* \frac{1}{\rho(\mathbf{r})} P^-(\mathbf{r}, \omega) \right]_{z_0} dx dy, \quad (2a)$$

where  $P^-$  and  $G^-$  represent the *upgoing parts* of the acoustic wavefield  $P$  at  $z = z_0$  and the Green's wavefield  $G$  at  $z = z_0$ , respectively. Note that the result of the preprocessing step is an upgoing wavefield at the surface.

The discrete version of this integral reads

$$P^-(\mathbf{r}_{A, ij}, \omega) = 2 \sum_{m=-\infty}^{\infty} \sum_{n=-\infty}^{\infty} \left[ \left( \frac{\partial G^-(\mathbf{r}_{mn}, \mathbf{r}_{A, ij}, \omega)}{\partial z} \right)^* \frac{\Delta x_m \Delta y_n}{\rho(\mathbf{r}_{mn})} P^-(\mathbf{r}_{mn}, \omega) \right]_{z=z_0}, \quad (2b)$$

where  $\mathbf{r}_{mn} = (x_m, y_n, z)$ ,  $\mathbf{r}_{A, ij} = (x_i, y_j, z_A)$ ,  $\Delta x_m = x_{m+1} - x_m$ , and  $\Delta y_n = y_{n+1} - y_n$ .

Equation (2b) is a 3D frequency-domain representation of the 'generalized Kirchhoff summation approach to inverse wavefield extrapolation'.

In analogy with Berkhout (1985) we can write this equation in the matrix notation

$$\bar{\mathbf{P}}^-(z_A) = \mathbf{F}_{\Pi}^-(z_A, z_0) \bar{\mathbf{P}}^-(z_0), \quad (3a)$$

where

$$\bar{\mathbf{P}}(z) = [P(x_1, y_1, z, \omega) \dots P(x_M, y_1, z, \omega) | P(x_1, y_2, z, \omega) \dots P(x_M, y_2, z, \omega) | \dots | P(x_1, y_N, z, \omega) \dots P(x_M, y_N, z, \omega)]^T,$$

containing the monochromatic pressure values  $P(x_m, y_n, z, \omega)$  for all  $(x_m, y_n)$  at depth  $z$ .

Fig. 3 shows this representation of the 2D and 3D version of the matrix notation. In Fig. 3a the 2D representation as introduced by Berkhout (1985) is shown. The vector  $\bar{\mathbf{P}}^-$  contains the 2D monochromatic wavefield at the lateral coordinates  $x$ . In this way inverse wavefield extrapolation can be described by a matrix multiplication with the extrapolation matrix  $\mathbf{F}_{\Pi}^-(z_A, z_0)$ . This matrix notation can be extended to 3D (Fig. 3b) by placing the 2D vectors for each  $y$ -value one after another in one vector (equation (3a)). So the index of the vector indicates a 2D coordinate in  $x$  and  $y$ . Note that we now have the same formulation for the 3D case as for the 2D case (except that the values for a 3D wavefield and for 3D extrapolation operators are of course different).

Hence the rows of  $\mathbf{F}_{\Pi}^-(z_A, z_0)$  contain

$$2 \left[ \left( \frac{\partial G^-(\mathbf{r}_{mn}, \mathbf{r}_{A, ij}, \omega)}{\partial z} \right)^* \frac{\Delta x_m \Delta y_n}{\rho(\mathbf{r}_{mn})} \right]_{z=z_0} \quad (3b)$$

for all  $(x_m, y_n)$  at depth  $z_0$  (i.e. the surface locations  $\mathbf{r}_{mn}$ ) and for one  $(x_i, y_j)$  at depth  $z_A$  (i.e. the locations  $\mathbf{r}_{A, ij}$  at the target's upper boundary).

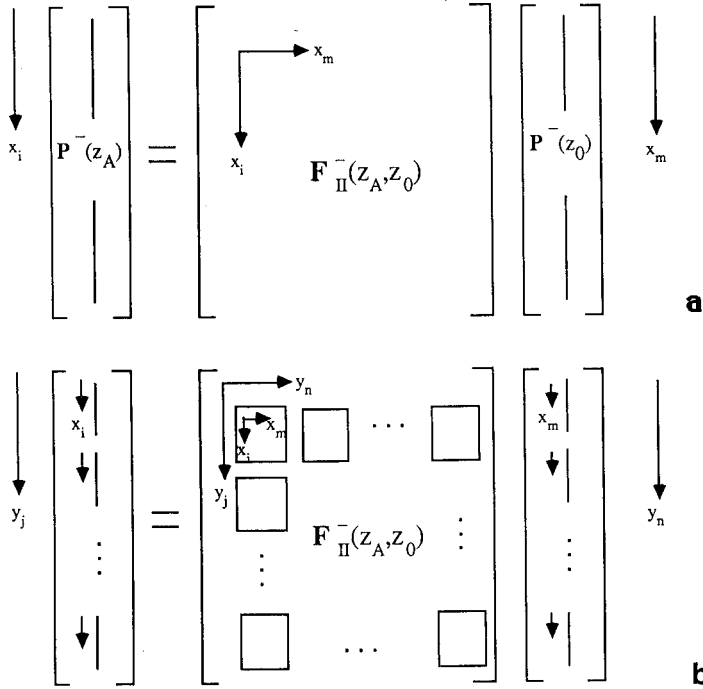


FIG. 3. The matrix notation for wavefield extrapolation. (a) 2D representation, (b) 3D representation.

Analogous to (3), for the forward extrapolation of the downgoing waves from  $z_0$  to  $z_A$  we can write

$$\tilde{P}^+(z_A) = W_{II}^+(z_A, z_0)\tilde{P}^+(z_0), \tag{4a}$$

where the rows of  $W_{II}^+(z_A, z_0)$  are given by

$$2 \left[ \left( \frac{\partial G^-(\mathbf{r}_{mn}, \mathbf{r}_A, ij, \omega)}{\partial z} \right) \frac{\Delta x_m \Delta y_n}{\rho(\mathbf{r}_{mn})} \right]_{z=z_0}. \tag{4b}$$

Notice that the Green's wavefield  $G(\mathbf{r}, \mathbf{r}_A, \omega)$  represents the response at  $\mathbf{r}$  of a point source at  $\mathbf{r} = \mathbf{r}_A$ . Hence extrapolation operators can be developed by a forward modelling scheme (see (3b) and (4b)). A very accurate way is to use a finite difference modelling scheme. Because we want to use the extrapolation operators in a 3D redatuming scheme, we now use a more efficient way of modelling Green's wavefields for constructing extrapolation operators, namely Gaussian beam modelling and ray tracing.

Wapenaar *et al.* (1989) give a detailed description of the (amplitude) errors in the expression for inverse wavefield extrapolation (2). They show that, assuming exact Green's functions, with (2) only the upgoing wavefield at  $\mathbf{r}_A$  is reconstructed. Evanescent waves are neglected and for an arbitrary inhomogeneous medium second-order amplitude errors are introduced. First-order amplitude effects, like geometrical

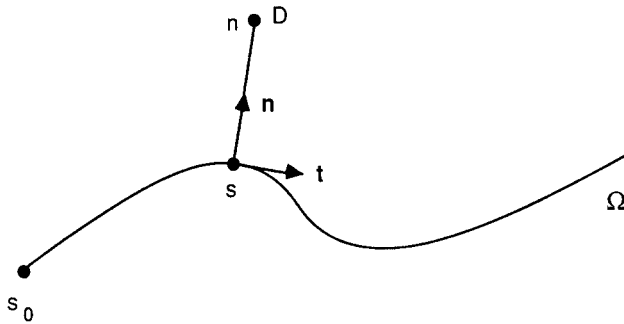


FIG. 4. Ray centred coordinate system along ray  $\Omega$  with coordinates  $s$  and  $n$ .

spreading and transmission at interfaces are incorporated correctly. In the following we will make further approximations by using a ray tracing method and a Gaussian beam method for the calculation of the Green's functions. We emphasize that, using moderate velocity variations, our operators describe non-recursive true-amplitude inverse wavefield extrapolation of primary waves.

### GAUSSIAN BEAMS

In this section we describe the Gaussian beam method as a modelling algorithm. As explained in the previous section, any forward modelling scheme can be used to calculate the Green's wavefields, that are used in the inverse wavefield extrapolation operators. It is beyond the scope of this paper to handle the complete Gaussian beam theory, but a basic discussion is necessary to understand the use of the Gaussian beam method in our inverse extrapolation algorithm. The main results from the theory are presented and especially the principles of Gaussian beam modelling are explained. For a thorough description we refer to Cerveny, Popov and Psencik (1982).

Gaussian beams are based on a solution of the wave equation (here the 2D acoustic wave equation) in a ray centred coordinate system with coordinates (see Fig. 4)  $s$  which measures the arclength along the ray ( $\Omega$ ) from an arbitrary reference point  $s_0$ ; and  $n$  which measures the distance perpendicular to the ray ( $\Omega$ ) from  $s$ .

The basis of the new ray centred coordinate system is formed by the independent unit vectors (Fig. 4)

$\mathbf{t}$  tangent to the ray in point  $(s, n = 0)$  and

$\mathbf{n}$  normal to the ray in point  $(s, n = 0)$ .

By using a high-frequency approximation, for the solution of the wave equation in the vicinity of the ray (following Cerveny, Popov and Psencik we can write

$$P(s, n, \omega) = \sqrt{\frac{v(s)}{q(s)}} \exp \left[ -i\omega \int_{s_0}^s \frac{ds}{v(s)} - \frac{i\omega}{2v(s)} K(s)n^2 - \frac{n^2}{L^2(s)} \right], \quad (5)$$

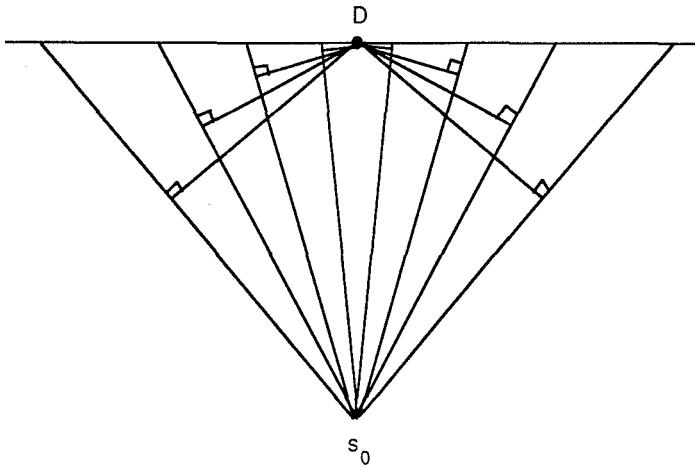


FIG. 5. Principle of the modelling scheme using the Gaussian beam method. Here the situation is shown for a source  $s_0$  and detector  $D$  in an homogeneous medium.

where  $v(s)$  is the propagation velocity along the ray,  $q(s)$  represents the geometrical spreading,  $K(s)$  can be interpreted as the curvature of the phase front of the beam, and  $L(s)$  represents the effective half-width of the beam. Note that  $q(s)$ ,  $K(s)$  and  $L(s)$  have, in general, complex values.

Gaussian beam modelling is based on the following principle:

1. At the source, decompose the wavefields into a number of Gaussian beams.
2. Trace each beam through the medium and determine the beam parameters  $v(s)$ ,  $q(s)$ ,  $K(s)$  and  $L(s)$ .
3. At any detector position, compute the contribution of the different beams by evaluating (5) for each beam and sum the results.

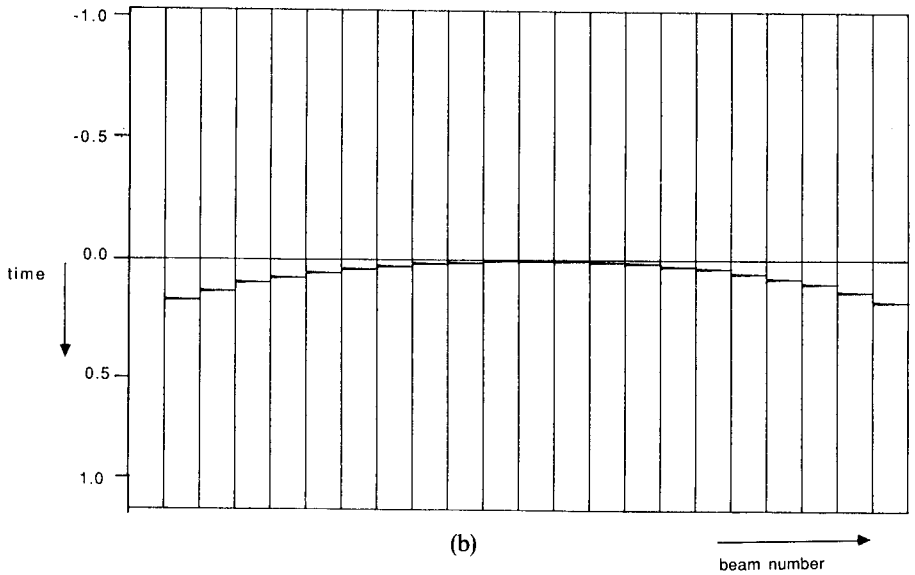
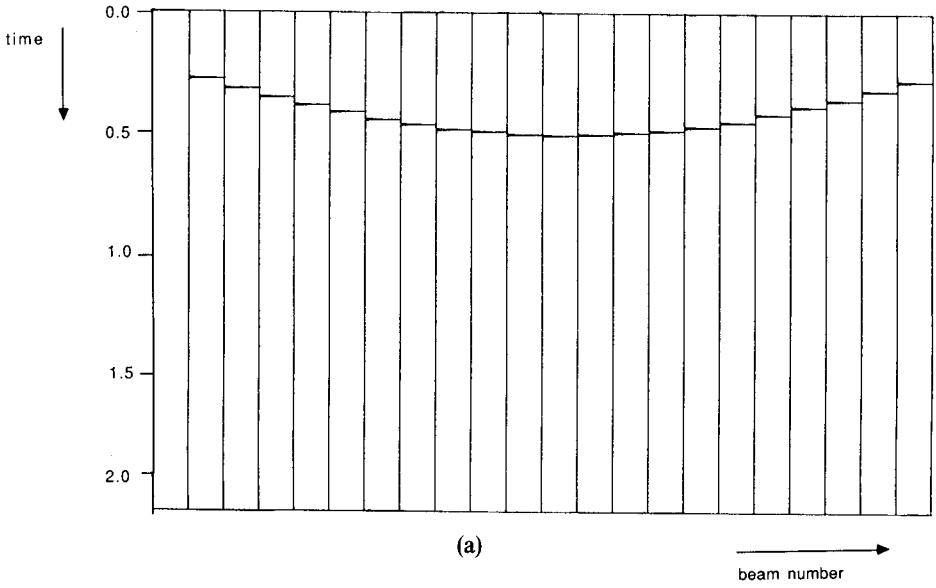
In Fig. 5 the response at detector  $D$  of a point source at  $s_0$  is schematically displayed as the summation over all contributing beams, which were shot with equidistant take-off angles. For the exact expressions of the parameters in (5) we refer again to Cerveny, Popov and Psencik (1982), but here we try to explain the physical meaning of each of the components with a simple example.

Again consider the geometry of Fig. 5 of a point source in a homogeneous medium. First consider the traveltime along each ray, which is described by the term

$$\exp \left[ -i\omega \int_{s_0}^s \frac{ds}{v(s)} \right], \quad (6a)$$

where  $\int \frac{ds}{v(s)}$  determines the traveltime.

These traveltimes are depicted in Fig. 6a as a function of the beam number. With an increasing distance of point  $D$  to the ray we have a decreasing traveltime. This is clear because we take the normal to each ray in  $s$ , see also Fig. 5.



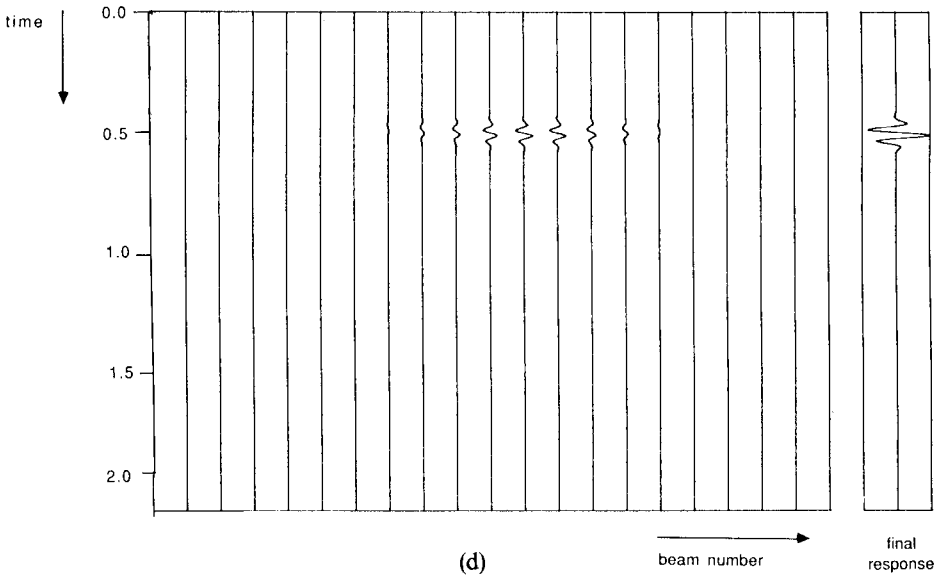
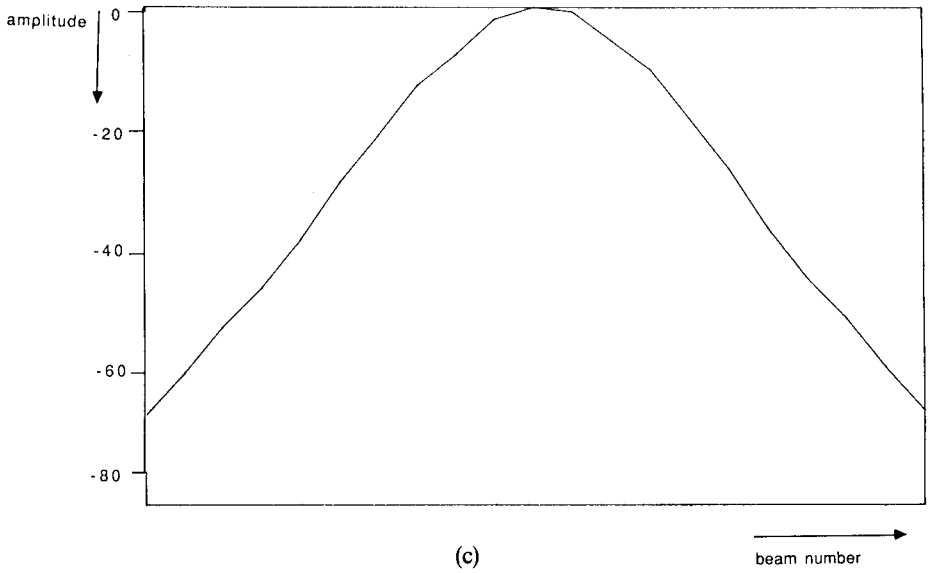


FIG. 6. Contributions per beam of the different terms in the Gaussian beam expression (5) to the total response. (a) Traveltime. (b) Wavefront curvature. (c) Amplitude. (d) Total contribution per beam convolved with a wavelet (left panel) and summed over all beams (right panel).

The second term accounts for the curvature of the wavefront

$$\exp \left[ - \frac{i\omega}{2v(s)} K(s)n^2 \right], \quad (6b)$$

where  $\text{Real}[\frac{1}{2}K(s)n^2/v(s)]$  determines a traveltime.

The contribution of this term to the total traveltime is shown in Fig. 6b. Here we have an increasing traveltime contribution for increasing distance  $n$ .

Finally we look at the amplitude term

$$\sqrt{\frac{v(s)}{q(s)}} \exp \left[ - \frac{n^2}{L^2(s)} \right]. \quad (6c)$$

This amplitude term is a Gaussian function of the normal distance  $n$ . For this reason the method is called the Gaussian beam method. This term is shown in Fig. 6c.

In Fig. 6d the combined contributions of (6a, b, c) are depicted per beam (convolved with a wavelet). These contributions are summed, yielding the response at detector point  $D$  of source  $S_0$  (Fig. 5), which is the trace on the right in Fig. 6d.

We have described the Gaussian beam method and we have shown how each beam contributes to the response at a certain detector point. To conclude this section we outline the procedure in a modelling scheme using the Gaussian beam method. This scheme is shown in Fig. 7.

For a certain take-off angle at the source a ray is calculated using a dynamic ray tracing method. Any inhomogeneous subsurface model can be used here. For each detector position the contribution of the ray is calculated. This is repeated for all rays, shot at equidistant take-off angles. The contributions of the rays are summed per detector position. In this way the wavefield at the detectors can be calculated from a point source. This method is stable in caustics and it has a correct amplitude behaviour. Also shadow zones, that form an important problem in dynamic ray tracing, are avoided in the Gaussian beam method.

The Gaussian beam method can be extended to 3D without much difficulty. For the 3D Gaussian beams the same advantages hold as for the 2D beams. It is an efficient method with a good amplitude behaviour. We have not yet implemented a 3D extension, but for the future this extension is envisaged.

## PRACTICAL IMPLEMENTATION

In this section we concentrate on how the ray tracing and the Gaussian beam schemes are implemented in an efficient way for calculating extrapolation operators. It will be shown that the two methods fit elegantly in one general operator calculation and extrapolation scheme. When implementing these methods for modelling Green's wavefields the following points should be remembered.

In our application we want to extrapolate prestack data, measured at the surface to the upper boundary of the target zone. In acquisition it is generally impossible to

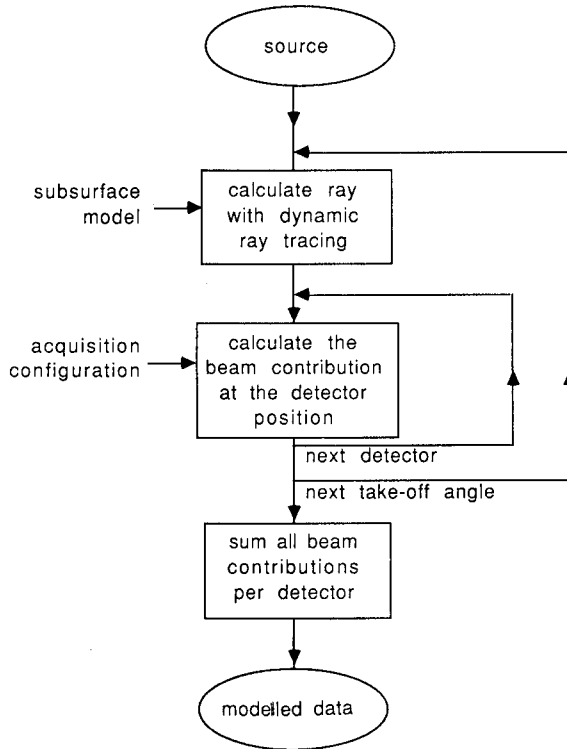


FIG. 7. The main steps in a modelling scheme, using Gaussian beams.

place the detectors (geophones for land data or hydrophones for marine data) on a regular grid. One tries to make the actual acquisition grid as regular as possible, but there will always be irregularities, e.g. due to roads and buildings or due to cable feathering in marine acquisition. In normal data processing it is often assumed that the acquisition points lie on a regular grid or instead the data is interpolated to a regular grid. By developing extrapolation operators for irregularly spaced acquisition geometries we can avoid contaminating the data by interpolation.

A second point, that can be advantageous in our scheme, is that for land acquisition most of the geophones are used for many shots. This means that for many shot records the same operator can be used to extrapolate the data. This is efficient because the operator has to be calculated just once. Unfortunately for marine acquisition this is not generally the case because of cable feathering.

A third point to keep in mind is that for the operator calculation one needs only the macro-subsurface model and the acquisition and target geometries. This makes it possible to calculate the operators in advance (before the redatuming itself) and to store the results on disc. We call this phase the operator development phase. During the actual extrapolation phase these results can be retrieved from disc. However, the operators for all frequencies would take too much disc space and would also result

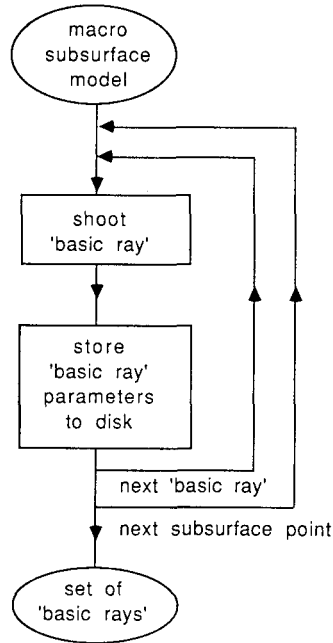


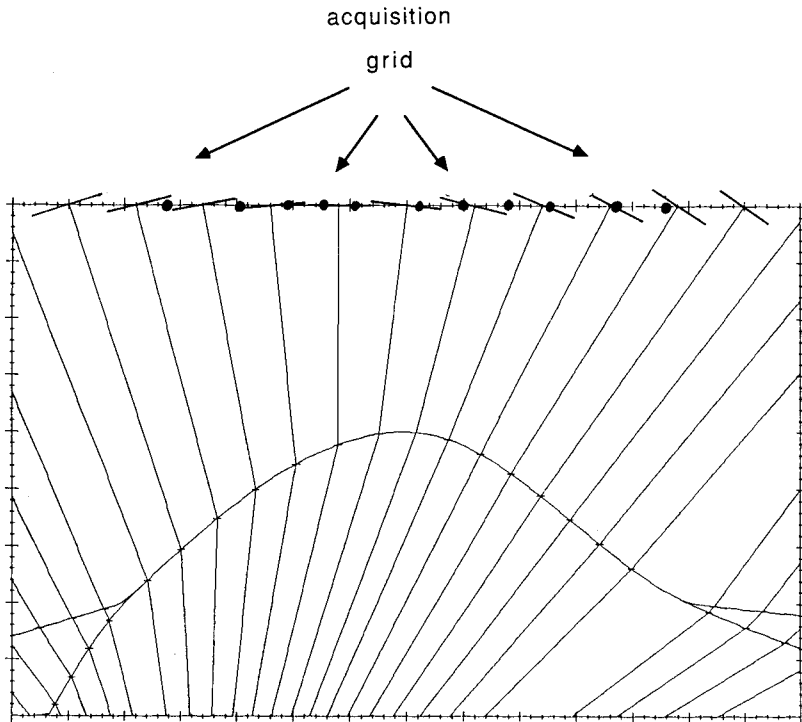
FIG. 8. The main steps in the scheme of the operator development phase.

in an inefficient I/O. Therefore we chose a method in which only a limited number of frequency-independent parameters need be stored after the operator development phase, and from which the actual operator can be calculated during the extrapolation phase.

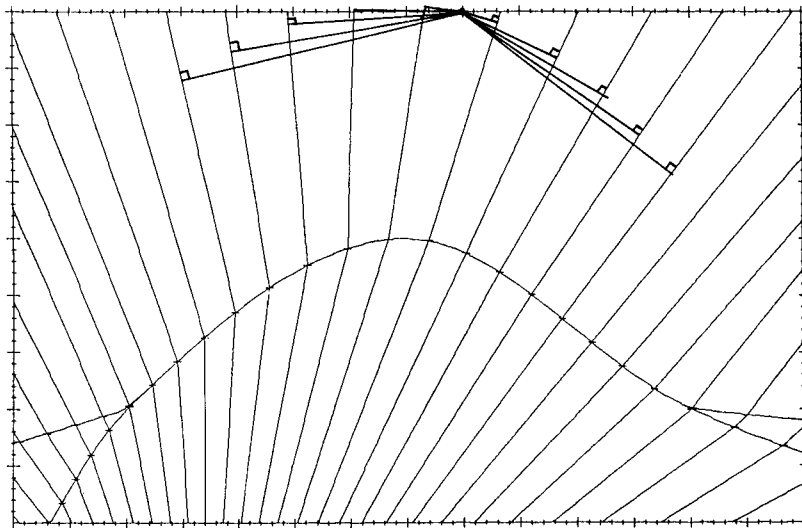
Considering these points we come to the scheme as shown in Figs 8 and 10. Notice that this scheme is independent of the method we choose for calculating the operators (either dynamic ray tracing or Gaussian beam modelling). Only the inner blocks of this scheme differ for the two methods.

The first part is the operator development phase (Fig. 8) and is performed separately from the actual extrapolation; it involves the calculation of the operator parameters. Using the macro-subsurface model, so called 'basic rays' are calculated from all positions at the upper boundary of the target zone to the surface. The actual acquisition grid is, as mentioned before, densely spaced and irregular. Later, during the extrapolation phase, the operator for the actual acquisition grid is calculated from these 'basic rays'. In the ray tracing method for this interpolation we use a Fraunhofer or local plane wave assumption. In the Gaussian beam method the theory describes the interpolation in a natural way.

In Fig. 9 the principles of these two methods are depicted schematically. For the ray tracing method the extrapolation operators are calculated through a correction to the parameters of the nearest ray(s), as depicted in Fig. 9a. The principle of the Gaussian beam method as depicted in Fig. 9b was discussed in the previous section.



(a)



(b)

FIG. 9. 'Operator interpolation' to the acquisition grid. (a) Ray tracing method: Local plane wave assumption. (b) Gaussian beam method: Sum over contributing rays.

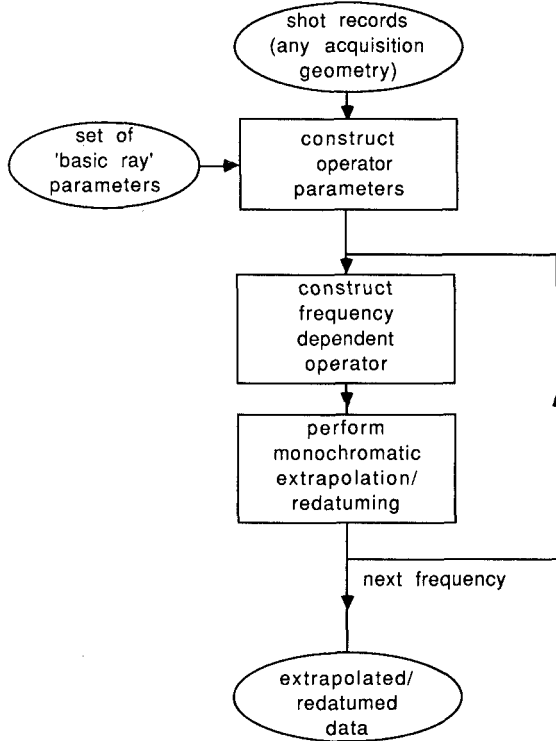


FIG. 10. The main steps in the scheme of the extrapolation phase.

By limiting the number of parameters to be stored to some characteristic parameters per ray, the amount of required disc space as well as the number of (time consuming) I/O operations (during the extrapolation phase) is greatly reduced.

The second stage of the calculation of the operator is done during the extrapolation phase, which is schematically depicted in Fig. 10. From the parameters of the 'basic rays' first the 'operator parameters' are constructed. These parameters are frequency-independent and contain the amplitude ( $A$ ) and traveltime ( $T$ ) information, that is needed to calculate the full operators, for all surface and target locations.

For dynamic ray tracing these frequency-independent operator parameters are obtained by applying a plane wave correction to the traveltime and amplitude of the nearest 'basic ray' to the actual acquisition point (see Fig. 9a). In 3D this correction is given by (see Fig. 11)

$$\Delta T = \frac{\sin \theta_g}{V_1} ((x_a - x_g) \cos \psi_g + (y_a - y_g) \sin \psi_g), \quad (7)$$

where  $(x_a, y_a)$  is the location of the acquisition point,  $\Delta T$  the correction to the traveltime of the 'basic ray',  $(x_g, y_g)$  is the location at the surface of the 'basic ray',  $\theta_g$  the dip angle at the surface of the 'basic ray',  $\psi_g$  the azimuth angle at the surface

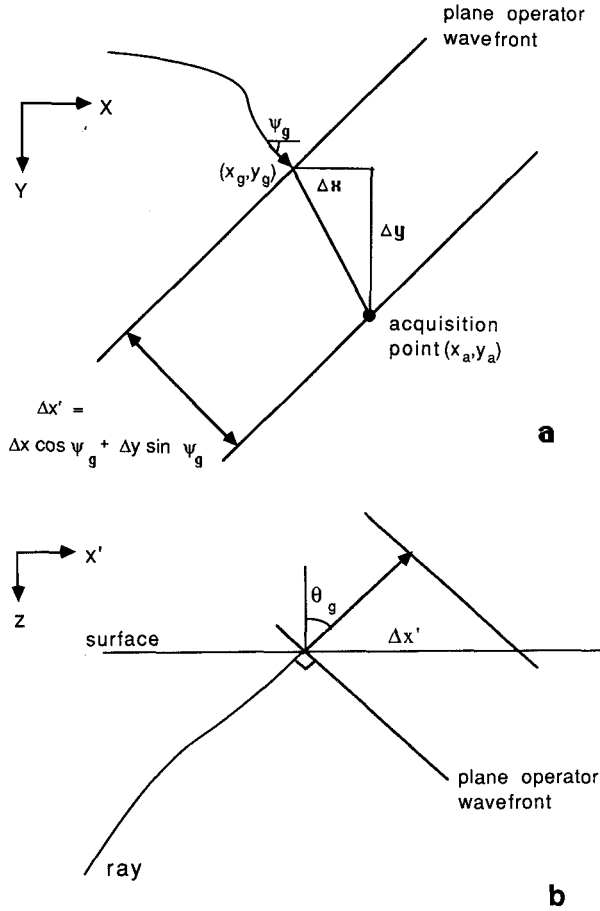


FIG. 11. Geometry for calculating the 3D Fraunhofer correction. (a) Top view. (b) Side view.

of the 'basic ray', and  $V_1$  the propagation velocity of the upper layer of the macro subsurface model.

Using a local plane wave or Fraunhofer approximation means that no amplitude correction is applied. The operator parameters  $T$  and  $A$  are stored in two 2D arrays (the two axes of these arrays represent the positions at the upper boundary of the target zone and the acquisition positions at the surface).

For Gaussian beam modelling the 'traveltime' and 'amplitude' information have complex values. The complex valued 'traveltime' contribution of one beam in a certain acquisition position can be described as

$$T(s, n) = \int_{s_0}^s \frac{ds}{v(s)} + \frac{1}{2v(s)} K(s)n^2, \tag{8a}$$

as can be deduced from (6a) and (6b).

The complex valued 'amplitude' for one beam at a certain acquisition point is given by

$$A(s, n) = \sqrt{\frac{v(s)}{q(s)}} \exp \left[ -\frac{n^2}{L^2(s)} \right], \quad (8b)$$

as in (6c). The complex operator parameters  $T$  and  $A$  are stored in two complex value 3D arrays. The three axes represent the positions at the upper boundary of the target zone, the acquisition positions at the surface and the beam number.

Within the frequency loop (see Fig. 10) the actual monochromatic extrapolation operator is finally calculated and the actual extrapolation is performed. Again the implementation of the operator construction differs for dynamic ray tracing and the Gaussian beam method, but the principles of the schemes are identical.

For the dynamic ray tracing method the monochromatic Green's function can be found from the operator parameters by

$$G^-(\mathbf{r}_{mn}, \mathbf{r}_{A, ij}, \omega) = A(\mathbf{r}_{mn}, \mathbf{r}_{A, ij}) e^{-i\omega T(\mathbf{r}_{mn}, \mathbf{r}_{A, ij})}. \quad (9a)$$

In the Gaussian beam method the monochromatic Green's function is calculated from the operator parameters by

$$G^-(\mathbf{r}_{mn}, \mathbf{r}_{A, ij}, \omega) = \sum_{b=1}^{\# \text{ beams}} A_b(\mathbf{r}_{mn}, \mathbf{r}_{A, ij}) e^{-i\omega T_b(\mathbf{r}_{mn}, \mathbf{r}_{A, ij})}. \quad (9b)$$

In both, the elements of the extrapolation operator  $F_{II}^-(z_A, z_0)$  follow directly from these Green's functions (see also (3b)). Just as in the operator development phase, in this extrapolation phase the implementation differs for the two methods, but the principles of the schemes (Fig. 10) are identical.

We now demonstrate this extrapolation scheme with two simple examples of inverse wavefield extrapolation applied to zero-offset data (redatuming of shot records is considered later).

The first example is a 2D subsurface model. Consider the model shown in Fig. 12a. Here a faulted structure is placed beneath a salt dome. Using the exploding reflector assumption and a finite difference modelling scheme, zero-offset data were generated at the surface from this faulted structure. Note that the reflections of the overlying layers were not modelled in this example.

In Fig. 12b the data obtained in this way are shown. The data were recorded at the surface from  $x = 0$  m to  $x = 1500$  m with a spacing of 9 m. From this data it is almost impossible to distinguish the faulted structure. Due to propagation through the overburden the image is heavily distorted.

With the ray tracing method the operators were calculated for an inverse extrapolation from the surface to a depth of 700 m, just above the faulted structure. In Fig. 13a the result after inverse extrapolation with the ray tracing method is shown. The propagation effects of the overburden are eliminated. The lateral positioning and the traveltimes of the extrapolated reflection are correct.

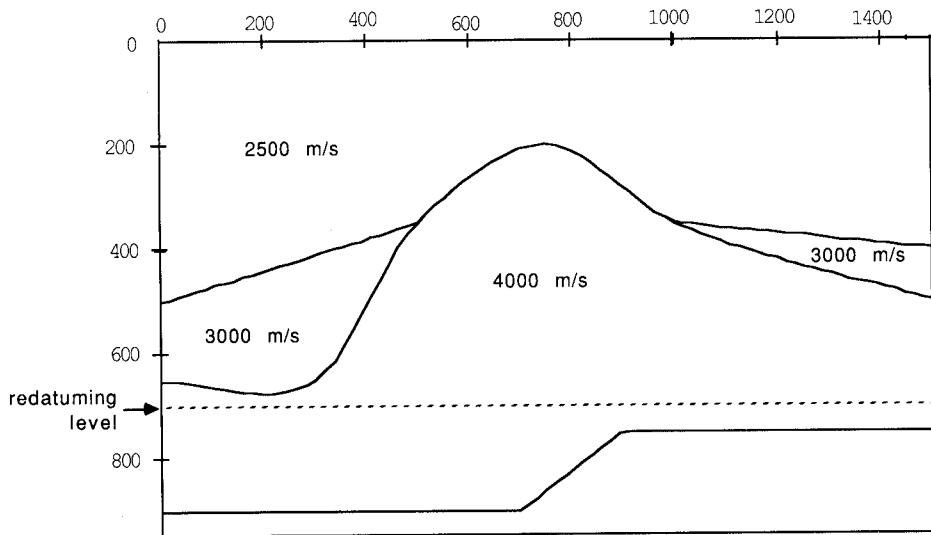


FIG. 12a. 2D subsurface model.

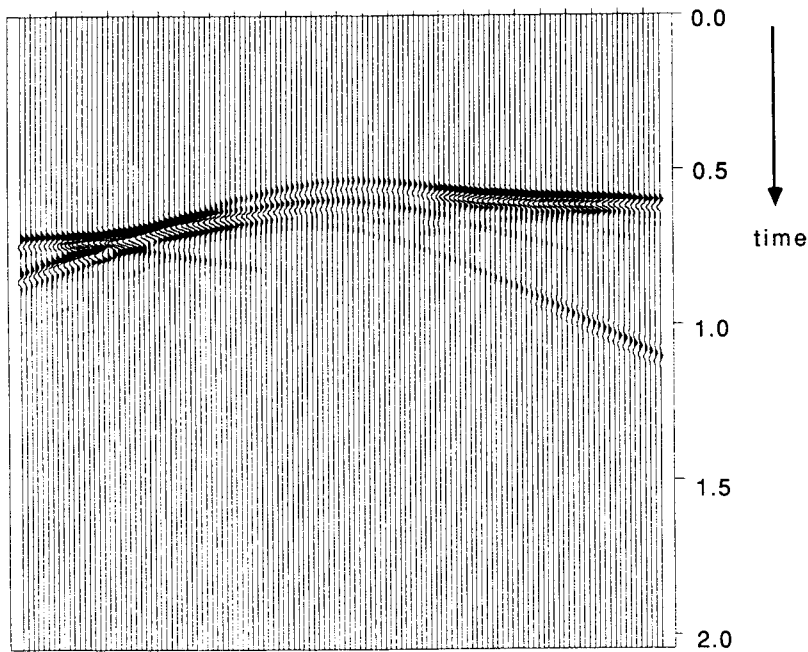


FIG. 12b. 2D zero-offset data from lower reflector, used as input for inverse wavefield extrapolation.

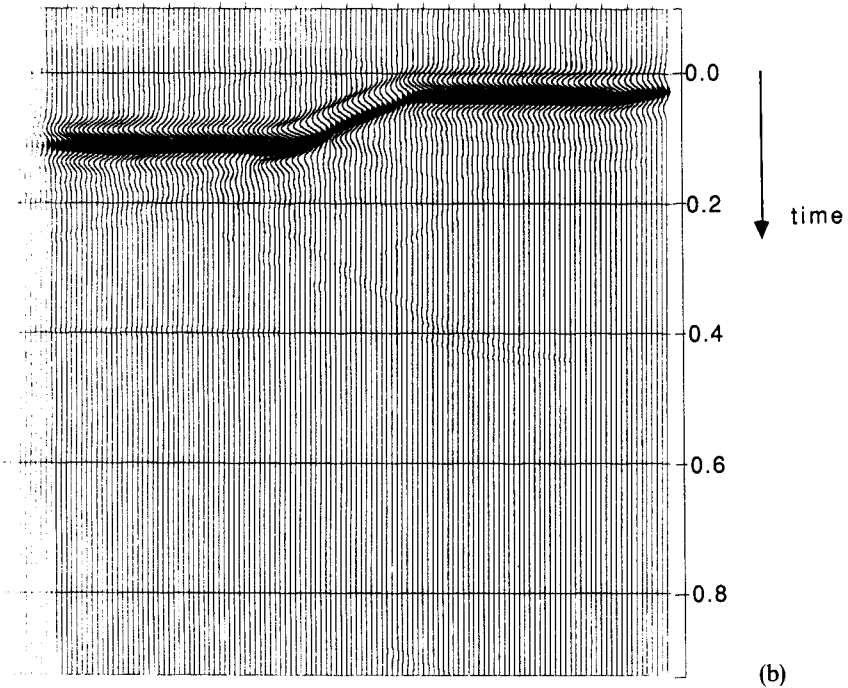
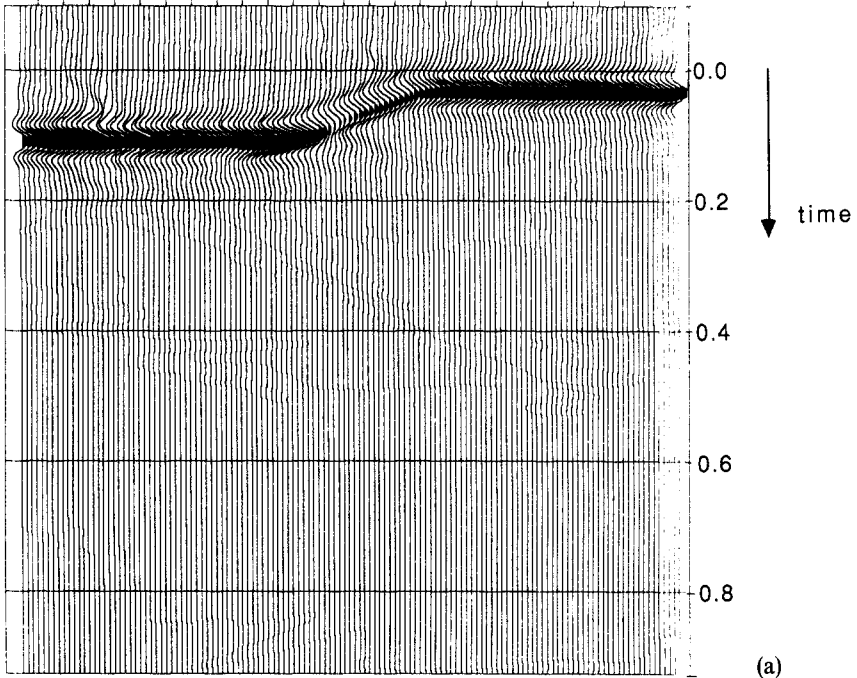


FIG. 13. Result after inverse extrapolation. (a) Using the ray tracing method. (b) Using the Gaussian beam method.

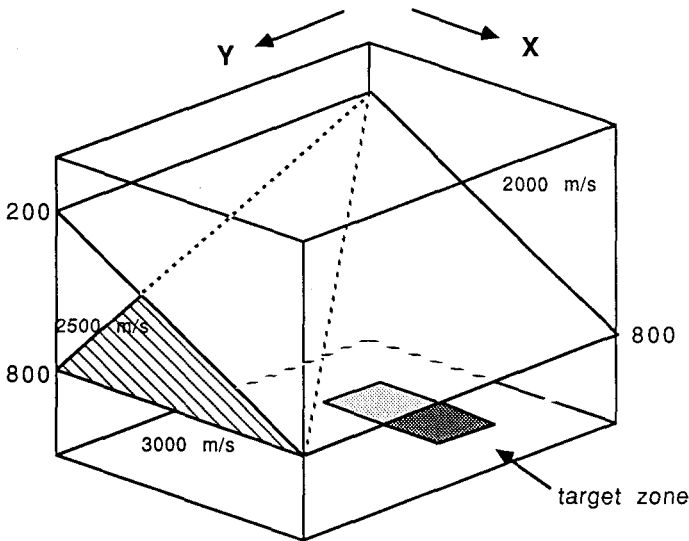


FIG. 14a. 3D subsurface model.

Using the Gaussian beam method for inverse wavefield extrapolation the amplitude behaviour is much better. The result is shown in Fig. 13b. Just as for the ray tracing method the position of the reflector is here correct. We see that the amplitude is smoother than for the ray tracing case. The side effects are also much smaller than for ray tracing. This is because the Gaussian beam method is based on the wave equation and does not suffer from shadow zones or instabilities.

The second example is a 3D inverse wavefield extrapolation. Here we only used the ray tracing based operators. In Fig. 14a the 3D inhomogeneous subsurface model is shown that was used for this example. With a recursive Kirchhoff modelling scheme zero-offset data was generated at the surface for a reflector of limited extent at a depth of 1000 m (see Fig. 14a). Two cross-sections of the data at the surface are shown in Fig. 14b. In Fig. 14c the result after 3D inverse wavefield extrapolation to  $z = 1000$  m is shown. The lateral positioning (both in the  $x$ - and in the  $y$ -direction) of the reflector is correct and the event aligns correctly at  $t = 0$  s.

In conclusion, we have developed a non-recursive inverse wavefield extrapolation scheme that is efficient with respect to computation time and I/O. It is possible to use this scheme to extrapolate through strongly inhomogeneous media for both 2D and 3D applications. In the following we show how to integrate this scheme in a shot record redatuming algorithm.

### THEORY OF REDATUMING

Following Berkhout (1985) the monochromatic response of a seismic experiment can be described by the following matrix formulation:

$$\vec{\mathbf{P}}_j^-(z_0) = \mathbf{D}(z_0) \left[ \sum_{m=1}^{\infty} \mathbf{W}^-(z_0, z_m) \mathbf{R}(z_m) \mathbf{W}^+(z_m, z_0) \right] \vec{\mathbf{S}}_j^+(z_0), \quad (10)$$

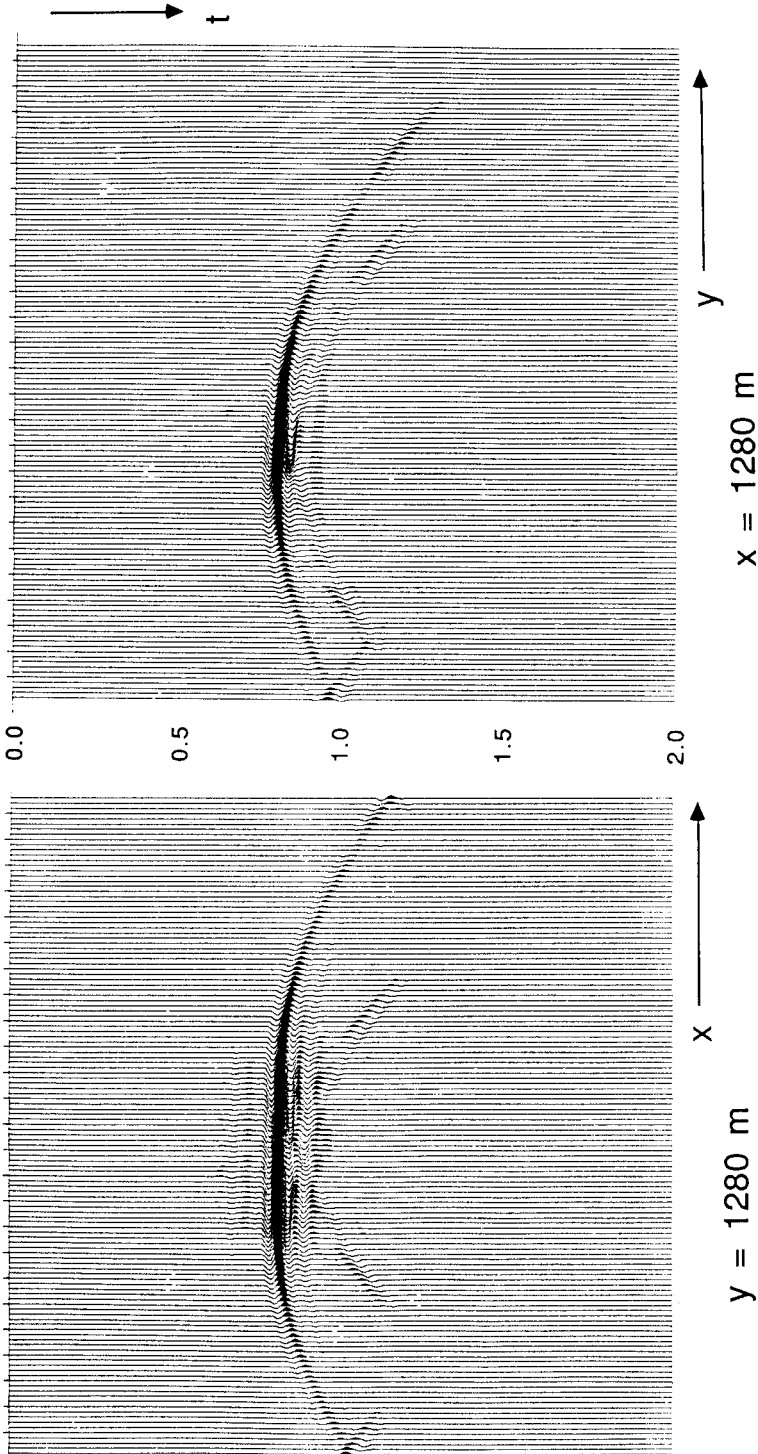


FIG. 14b. Two cross-sections through the data at the surface.

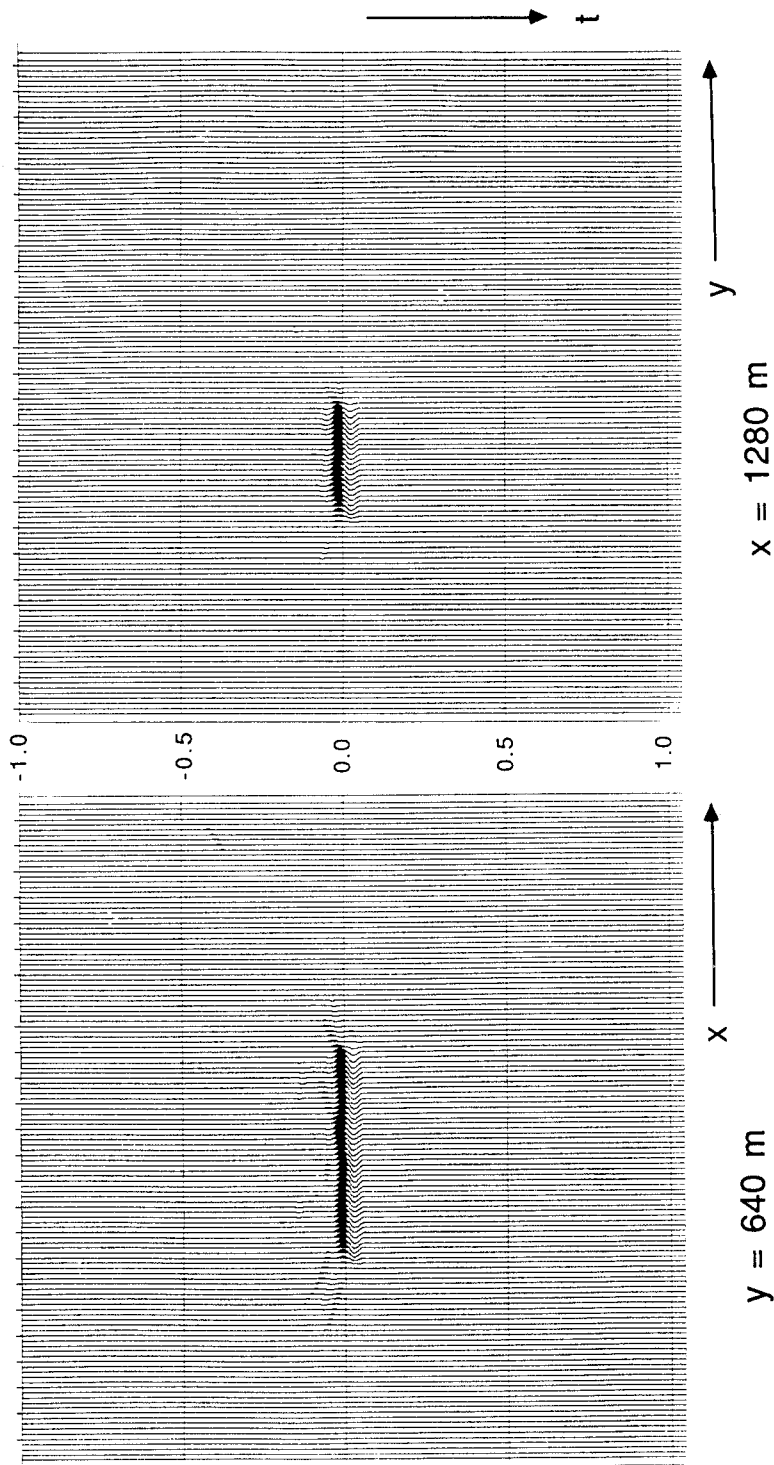


FIG. 14c. Two cross-sections through the data after 3D inverse wavefield extrapolation.

where  $\tilde{\mathbf{S}}_j^+(z_0)$  is a vector containing the downgoing source wavefield at the surface of source  $j$ ,  $\mathbf{W}^+(z_m, z_0)$  is a matrix describing the forward propagation of the downgoing wavefield from  $z_0$  to  $z_m$ ,  $\mathbf{R}(z_m)$  is a matrix describing the angle-dependent reflection properties at  $z_m$ ,  $\mathbf{W}^-(z_0, z_m)$  describes the forward propagation of the upgoing wavefield from  $z_m$  to  $z_0$ ,  $\mathbf{D}(z_0)$  describes the detector characteristics, and  $\tilde{\mathbf{P}}_j^-(z_0)$  is a vector containing the detected upgoing wavefield at  $z_0$  related to source  $j$ .

Notice that (10) describes a 2D or a 3D seismic experiment when the notation is used that is explained in Fig. 3a or 3b, respectively.

Equation (10) describes a single shot experiment. Extending this formulation to the multi-shot situation we have.

$$\mathbf{P}^-(z_0) = \mathbf{D}(z_0) \left[ \sum_{m=1}^{\infty} \mathbf{W}^-(z_0, z_m) \mathbf{R}(z_m) \mathbf{W}^+(z_m, z_0) \right] \mathbf{S}^+(z_0), \quad (11)$$

where the columns of matrices  $\mathbf{P}^-(z_0)$  and  $\mathbf{S}^+(z_0)$  represent the single shot wavefields  $\tilde{\mathbf{P}}_j^-(z_0)$  and  $\tilde{\mathbf{S}}_j^+(z_0)$  for  $j = 1 \dots J$ .

For simplicity, in the rest of this paper we assume that  $\mathbf{D}(z_0)$  can be inverted (i.e. directional deconvolution) and that we can omit this term.

If we let the upper boundary of the target zone be at  $z = z_N$ , we can write (10) as

$$\begin{aligned} \tilde{\mathbf{P}}_j^-(z_0) = & \left[ \sum_{m=1}^{N-1} \mathbf{W}^-(z_0, z_m) \mathbf{R}(z_m) \mathbf{W}^+(z_m, z_0) \right] \mathbf{S}_j^+(z_0) \\ & + \mathbf{W}^-(z_0, z_N) \mathbf{X}(z_N) \mathbf{W}^+(z_N, z_0) \mathbf{S}_j^+(z_0), \end{aligned} \quad (12a)$$

where

$$\mathbf{X}(z_N) = \sum_{m=N}^{\infty} \mathbf{W}^-(z_N, z_m) \mathbf{R}(z_m) \mathbf{W}^+(z_m, z_N), \quad (12b)$$

$$\mathbf{W}^-(z_0, z_m) = \mathbf{W}^-(z_0, z_N) \mathbf{W}^-(z_N, z_m) \quad \text{for } m \geq N, \quad (12c)$$

and

$$\mathbf{W}^+(z_m, z_0) = \mathbf{W}^+(z_m, z_N) \mathbf{W}^+(z_N, z_0) \quad \text{for } m \geq N. \quad (12d)$$

Here  $\mathbf{X}(z_N)$  is the multi-dimensional spatial impulse response at  $z = z_N$  of the sub-surface below  $z = z_N$ .

We see that relation (12a) is split into two major parts. The first part describes the response of the overburden. For redatuming we are not interested in this response. The geologist will be interested in the response of the target zone and this response is included in the second part of relation (12a).

In the measurements at the surface the impulse response ( $\mathbf{X}(z_N)$ ) at the target upper boundary is distorted by the propagation through the overburden (12a). This is described by the two propagation matrices  $\mathbf{W}^+(z_N, z_0)$  for the downward propagation of the source wavefield and  $\mathbf{W}^-(z_0, z_N)$  for the upward propagation of the reflected wavefield. Now we can give a more formal description of redatuming than the one given in the introduction. The aim of redatuming is to estimate  $\mathbf{X}(z_N)$ , which

involves elimination of the distorting effect of propagation (described by the matrices  $\mathbf{W}^+(z_N, z_0)$  and  $\mathbf{W}^-(z_0, z_N)$ ) through the overburden. Furthermore, for efficiency reasons we want to perform the redatuming per shot record.

First we derive the expressions for the full prestack redatuming, before handling the shot record redatuming. We follow the approach of Berkhout (1984) and Wapeenaar and Berkhout (1987).

Ignoring the response of the overburden, for the multi-shot record data we can write

$$\mathbf{P}^-(z_0) = \mathbf{W}^-(z_0, z_N)\mathbf{X}(z_N)\mathbf{W}^+(z_N, z_0)\mathbf{S}^+(z_0). \quad (13)$$

From this equation it is clear that the full prestack redatuming can be written as

$$\mathbf{P}^-(z_N) = \mathbf{F}^-(z_N, z_0)\mathbf{P}^-(z_0), \quad (14a)$$

$$\mathbf{S}^+(z_N) = \mathbf{W}^+(z_N, z_0)\mathbf{S}^+(z_0), \quad (14b)$$

and

$$\mathbf{X}(z_N) = \mathbf{P}^-(z_N)[\mathbf{S}^+(z_N)]^{-1}, \quad (14c)$$

where

$$\mathbf{F}^-(z_N, z_0) = [\mathbf{W}^-(z_0, z_N)]^{-1}. \quad (14d)$$

Equation (14) practically describes three steps in the redatuming scheme: (i) (14a) describes the inverse extrapolation of the detected upgoing wavefields  $\mathbf{P}^-(z_0)$  to  $z_N$ , (ii) (14b) describes the forward extrapolation of the downgoing source wavefields  $\mathbf{S}^+(z_0)$  to  $z_N$ , and finally (iii) the upgoing reflected wavefields  $\mathbf{P}^-(z_N)$  are deconvolved for the downgoing incident wavefields  $\mathbf{S}^+(z_N)$  at  $z = z_N$ , which is described in (14c).

For simplicity we will further assume that for the downgoing source wavefield we can write

$$\mathbf{S}^+(z_0) = S(\omega)\mathbf{I}, \quad (15)$$

where  $\mathbf{I}$  is the identity matrix and  $S(\omega)$  the spectrum of the source wavefield.

Now we can write for the deconvolution step (14c):

$$\mathbf{X}(z_N) = \mathbf{P}^-(z_N)[\mathbf{Z}^+(z_N)]^T, \quad (16a)$$

where

$$[\mathbf{Z}^+(z_N)]^T = \frac{[\mathbf{S}^+(z_0)]^{*T}}{\|S(\omega)\|^2} \mathbf{F}^+(z_0, z_N) \quad (16b)$$

and

$$\mathbf{F}^+(z_0, z_N) = [\mathbf{W}^+(z_N, z_0)]^{-1}. \quad (16c)$$

The bottom part of Fig. 15 illustrates the matrix multiplication of equation (16a).

Now that we have described the full prestack redatuming scheme with (14a), (16b) and (16a), we can describe the shot record redatuming. We do this with a 2D example. In this example we use the same subsurface model as before (Fig. 12a). The

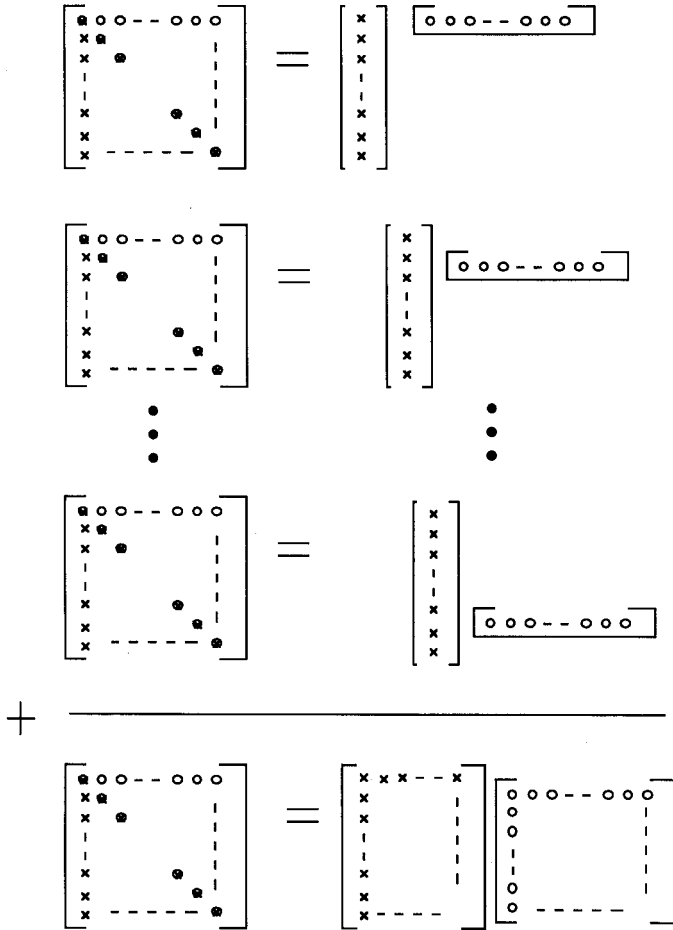


FIG. 15. Matrix representation of shot record redatuming (top) versus full prestack redatuming (bottom).

operators for this example are calculated with our ray tracing scheme. For this model shot records were generated using a finite difference modelling algorithm. In Fig. 16 one of the modelled shot records is shown for the lateral source position  $x = 500$  m.

The first step in the shot record redatuming scheme is equivalent to an inverse extrapolation of the detected wavefield. This is the single-shot record version of (14a):

$$\tilde{\mathbf{P}}_j^-(z_N) = \mathbf{F}^-(z_N, z_0)\tilde{\mathbf{P}}_j^-(z_0). \tag{17a}$$

Equations (17a and b) describe shot record redatuming per monochromatic component. The results of each step are plotted in the time domain after an inverse

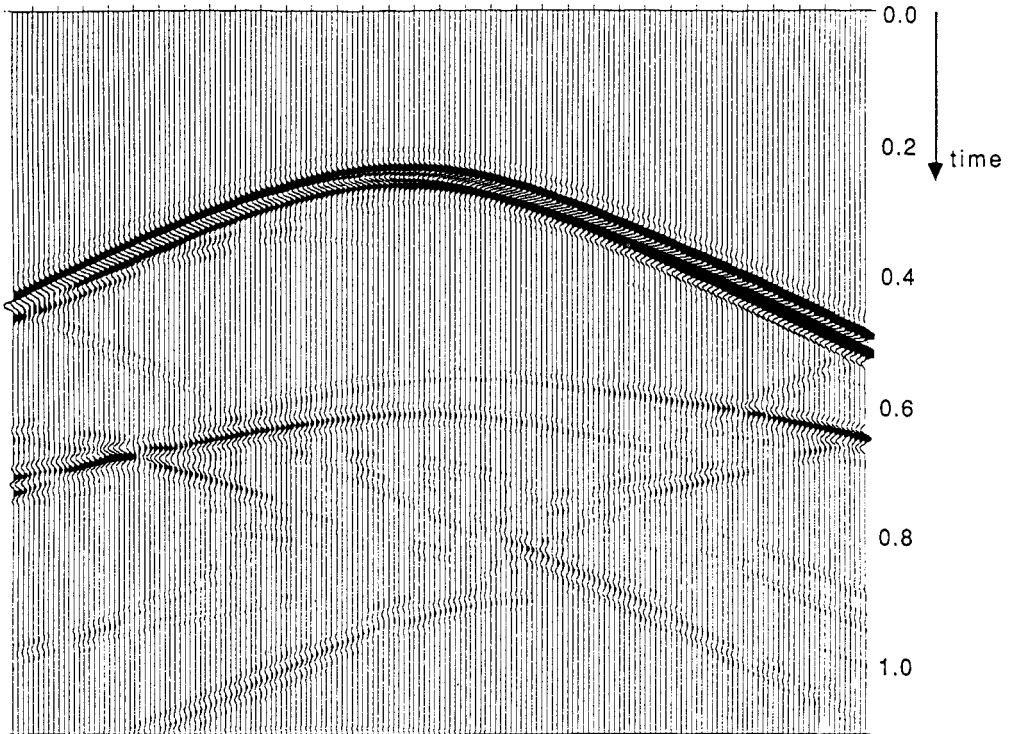


FIG. 16. Shot record for a source at  $x = 500$  m in the model of Fig. 12a.

Fourier transformation from frequency to time. The result of step (17a) is shown in Fig. 17a. The reflection of the lower reflector now becomes more clear. The second step is the single-shot record version of (16b):

$$[\bar{\mathbf{Z}}_j^+(z_N)]^T = \frac{[\bar{\mathbf{S}}_j^+(z_0)]^{*T}}{\|S(\omega)\|^2} \mathbf{F}^+(z_0, z_N). \tag{17b}$$

This step is comparable (for homogeneous media even equivalent) to the complex conjugate of the forward extrapolated source wavefield. In Fig. 17b the result of the forward extrapolated source field is shown.

The third step consists of a 'deconvolution' of the upgoing reflected wavefield (Fig. 17a) for the downgoing source wavefield (Fig. 17b) at the upper boundary of the target zone

$$\langle \mathbf{X}(z_N) \rangle_j = \bar{\mathbf{P}}_j^-(z_N) [\bar{\mathbf{Z}}_j^+(z_N)]^T. \tag{17c}$$

The result of this step is a single-fold redatumed section. In Fig. 17c the diagonal elements, corresponding to zero-offset, of this single-fold result are shown. Note that mainly the middle part of the lower reflector is illuminated by this shot at  $x = 500$  m.

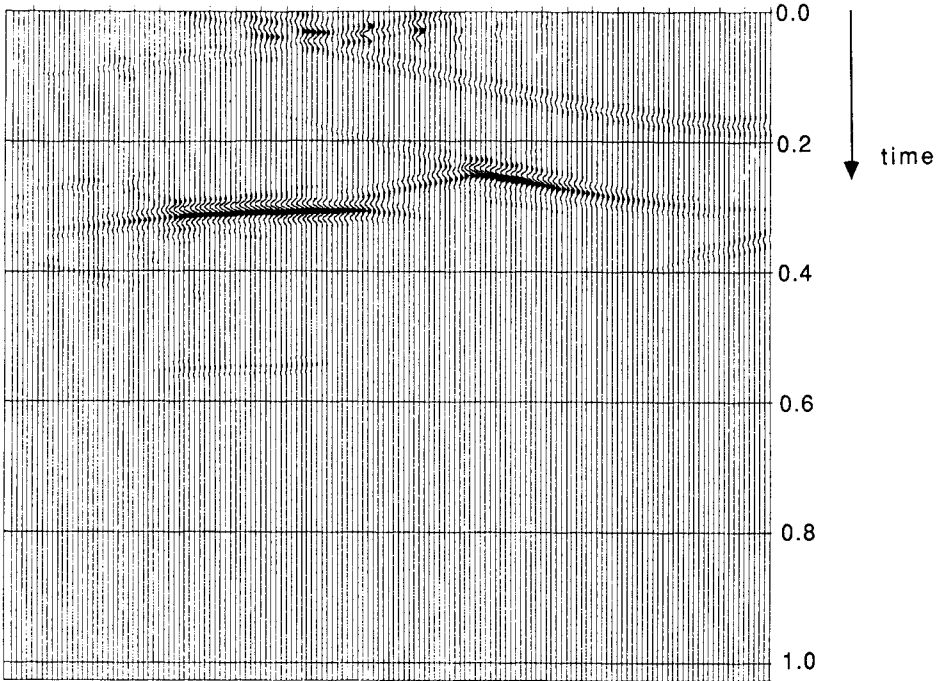


FIG. 17a. Inverse extrapolated detected wavefield at  $z = 700$  m.

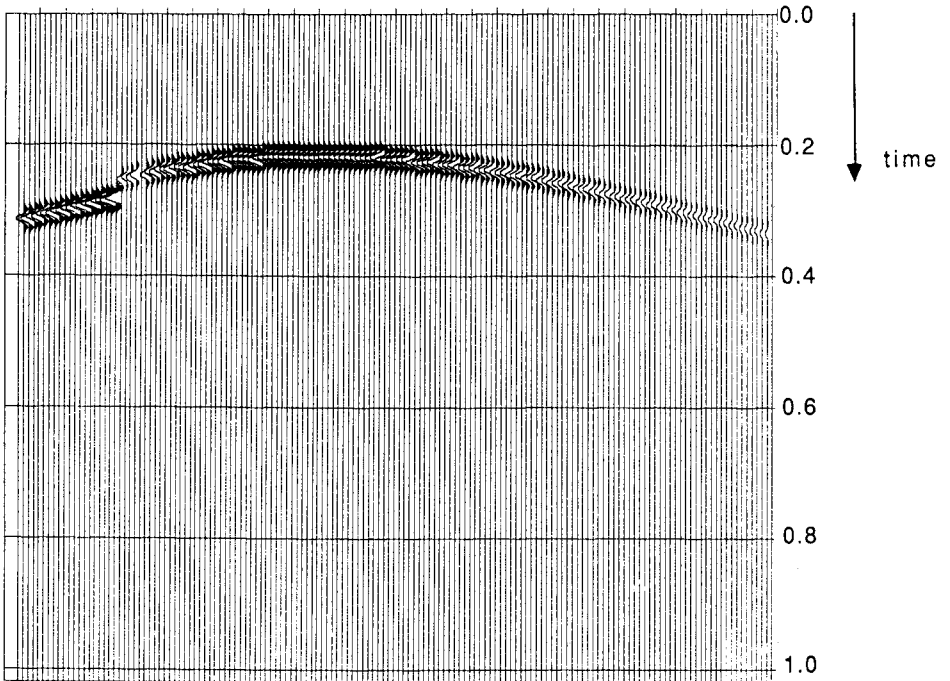


FIG. 17b. Forward extrapolated source wavefield at  $z = 700$  m.

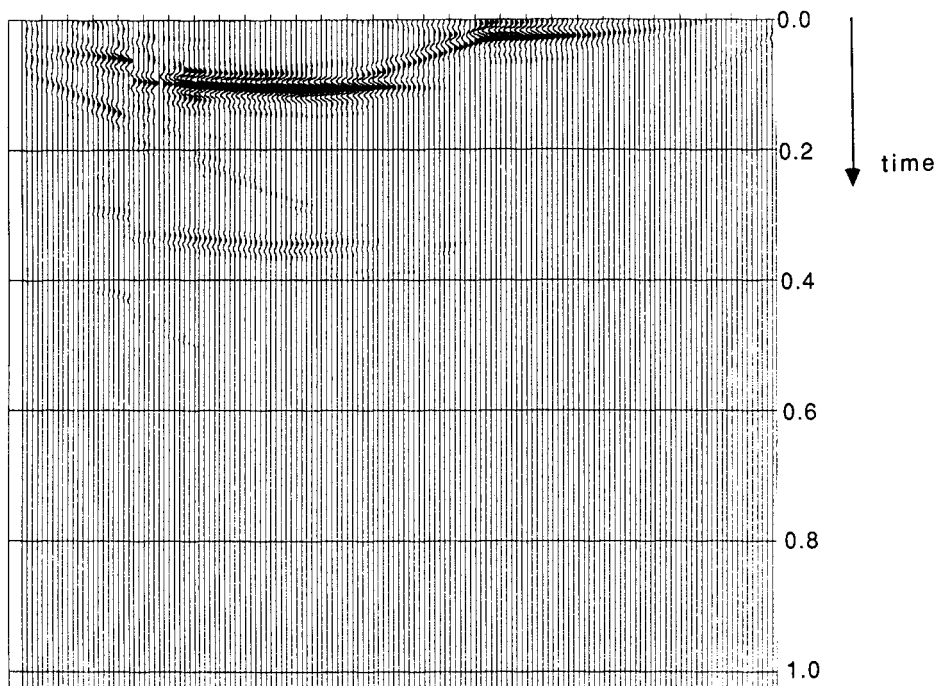


FIG. 17c. Single-fold redatumed section at  $z = 700$  m for a shot at  $x = 500$  m.

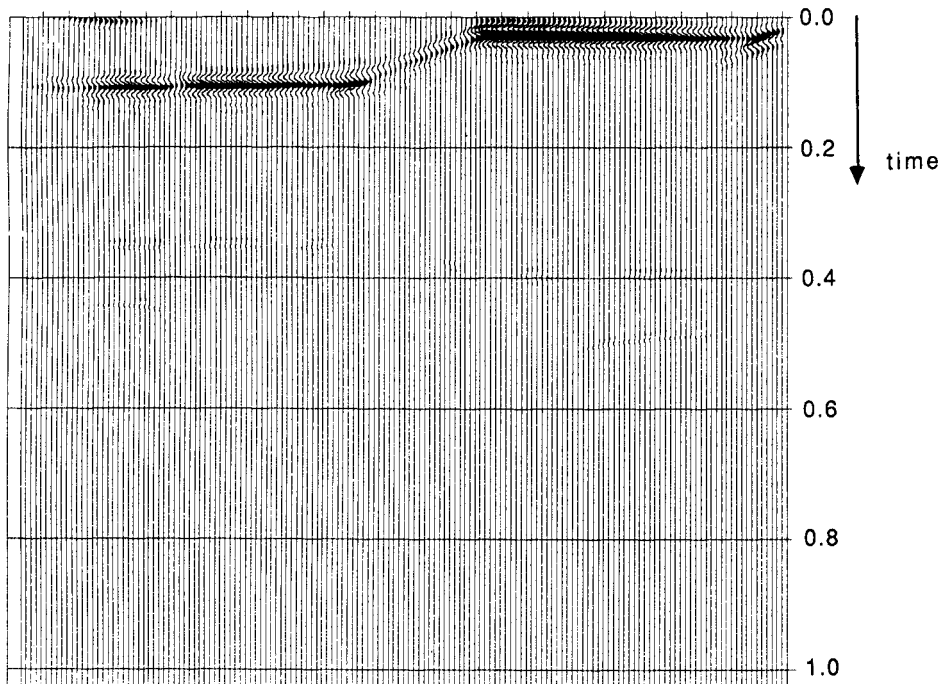


FIG. 17d. Genuine zero-offset response at  $z = 700$  m. Result after CMP stacking of all redatumed shot records.

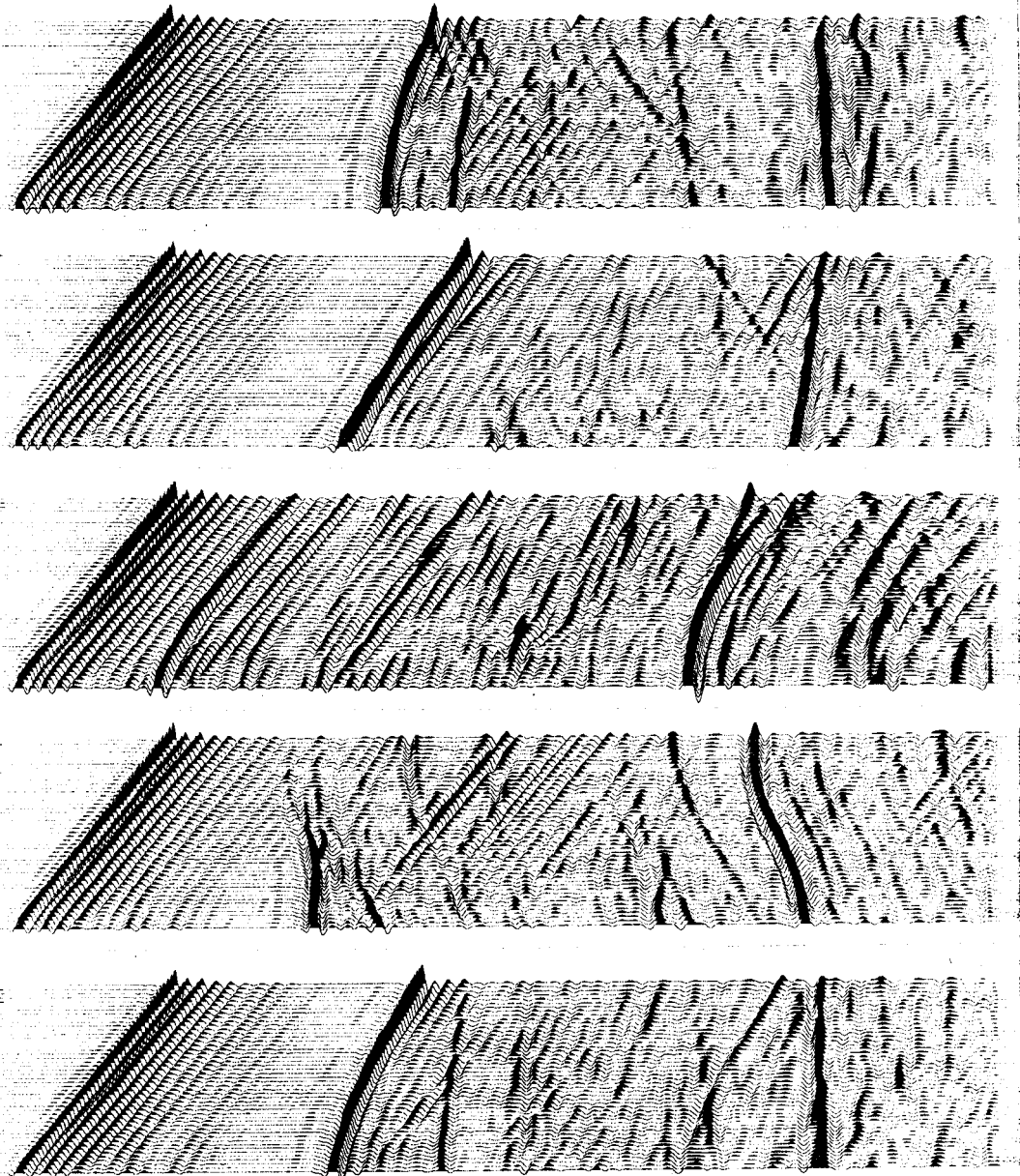


FIG. 18a. A shot record measured over a watertank model. (Courtesy Marathon Oil Comp.)

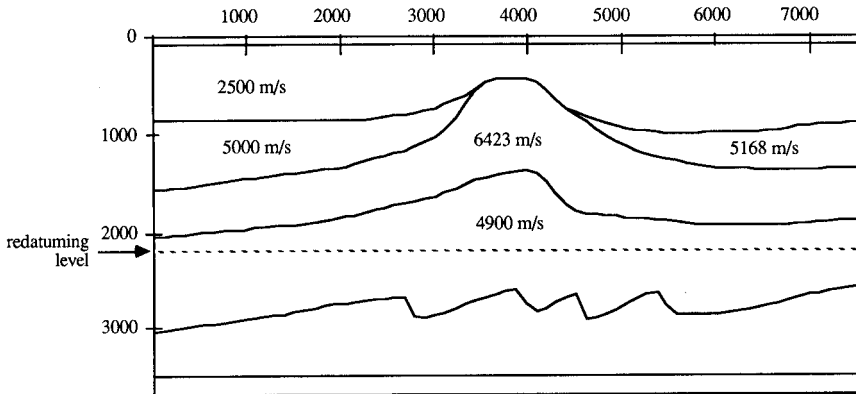


FIG. 18b. Estimated macro-subsurface model.

The final step in the redatuming process is the CMP stacking:

$$\mathbf{X}(z_N) = \sum_j \langle \mathbf{X}(z_N) \rangle_j. \quad (17d)$$

Here the redatuming results from all single shot records are summed, giving a data set as if it had been measured at the upper boundary of the target zone. Figure 15 shows that the result of shot record redatuming followed by stacking (17a, 17b, 17c and 17d) is exactly the same as full prestack redatuming (14a, 16b and 16a). The size of this data set would be of the same order as the original data set. However, the output can be limited to the diagonal elements of  $\mathbf{X}(z_N)$ , resulting in a genuine zero-offset response as shown in Fig. 17d. By not calculating the off-diagonal elements of  $\mathbf{X}(z_N)$  the size of the data volume is reduced considerably. Also the number of calculations to be done for the 'deconvolution' (17c) is reduced. It can be seen that the quality of this zero-offset data at the target is far better than could be reached with a conventional CMP stacking at the surface.

## 2D AND 3D REDATUMING EXAMPLES

In this section we describe another two examples of the redatuming scheme. The first example is redatuming of a 2D watertank experiment. The experiments and some results obtained with these data were described by Postma and Jeannot (1988). In Fig. 18a some shot records obtained over the model are shown. From the shot records a macro-subsurface model was derived with a focusing analysis method, described by Cox *et al.* (1988). This estimated model is shown in Fig. 18b. The result after shot record redatuming to  $z = 2200$  m is shown in Fig. 18c. We see that the lower reflectors are recovered well. Due to the propagation velocities in the target zone the lower reflector is not horizontal in the time domain.

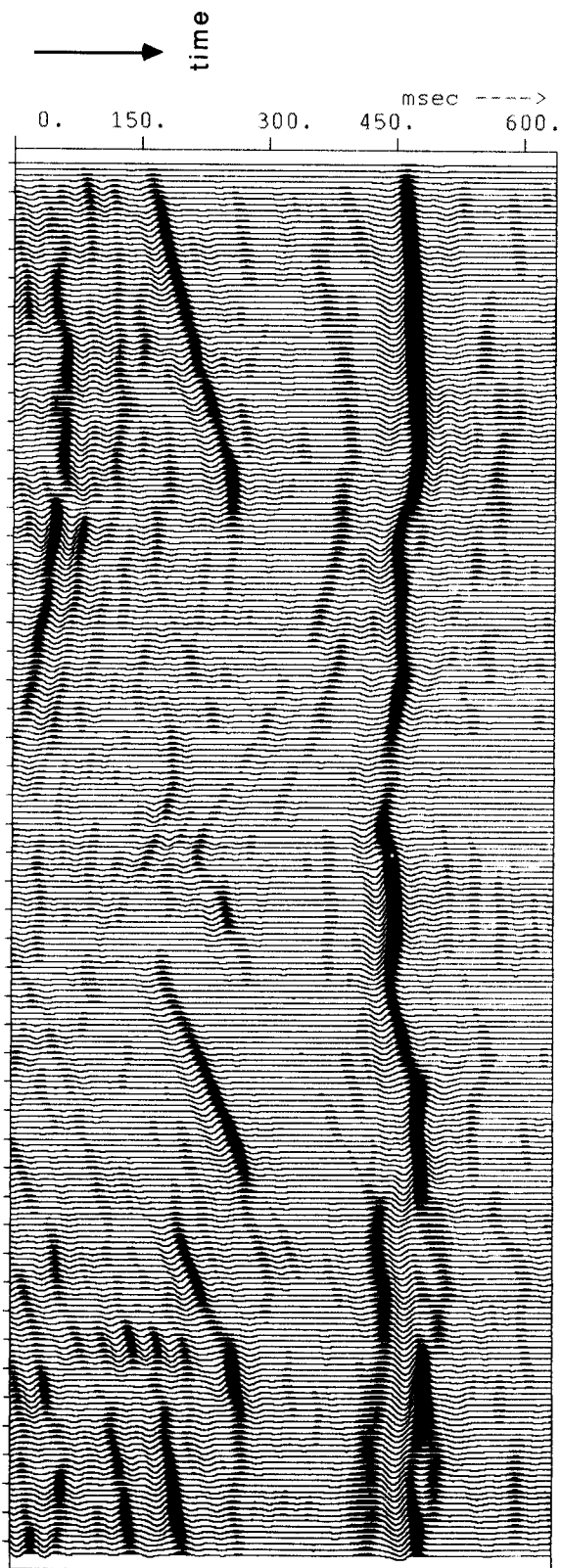


FIG. 18c. Result after redatuming to  $z = 2200$  m.

The second example is a redatuming of a 3D prestack data set, modelled with ray tracing. In Fig. 19a a perspective view of the 3D subsurface model is given. Note that the model has lateral variations in both the  $x$ - and  $y$ -direction. In Fig. 19b two cross-sections through the model are shown. Using ray tracing, shot records were generated at the surface with the response of five point diffractors at  $z = 1000$  m. The reflections of the layers in the overburden were not modelled in this example. Figure 19c shows some cross-sections through the data of two shot records as indicated in Fig. 19a.

Using 3D shot record redatuming, zero-offset data were generated at  $z = 1000$  m, the level of the point diffractors. Figure 19d shows four cross-sections through the zero-offset data. The positions of these cross-sections are also indicated in Fig. 19a. We see that all point diffractors are focused correctly and they are positioned at  $t = 0$  s and at the correct position in  $x$  and  $y$ . This example shows that, with the method described in this paper, correct 3D redatuming is possible. The method is efficient and makes 3D prestack processing feasible on modern supercomputers.

## CONCLUSIONS

We have described a method for the redatuming of shot records. Especially for 3D shot records, the scheme that is used to calculate and apply wavefield extrapolation operators must be efficient. We have presented two procedures, based on ray tracing and Gaussian beams, respectively.

In an example of 2D inverse wavefield extrapolation, both methods proved to be efficient and flexible. Non-recursive extrapolation operators can be generated for any type of inhomogeneous overburden. Also any irregular shooting geometry can be handled by these two schemes. Both methods have good focusing and positioning properties. As expected, the amplitude behaviour of the Gaussian beam method is better than the amplitude behaviour of the operators obtained by ray tracing.

For 3D wavefield extrapolation the Gaussian beam method has not yet been implemented, but here the ray tracing method also proved to be successful. When using a 3D Gaussian beam method the results should improve in the same way as in the 2D example.

We have discussed a shot record redatuming scheme in which we integrated the ray tracing based extrapolation operators. The redatuming is performed per shot record which has, especially for the 3D redatuming, the advantage over the conventional redatuming scheme, that no reordering of the data is needed. Because the extrapolation is done non-recursively no padding of far-offset traces before extrapolation is needed. This is in contrast to shot record migration schemes. Hence, with our shot record approach to prestack redatuming, 3D seismic processing before stack becomes feasible on modern supercomputers.

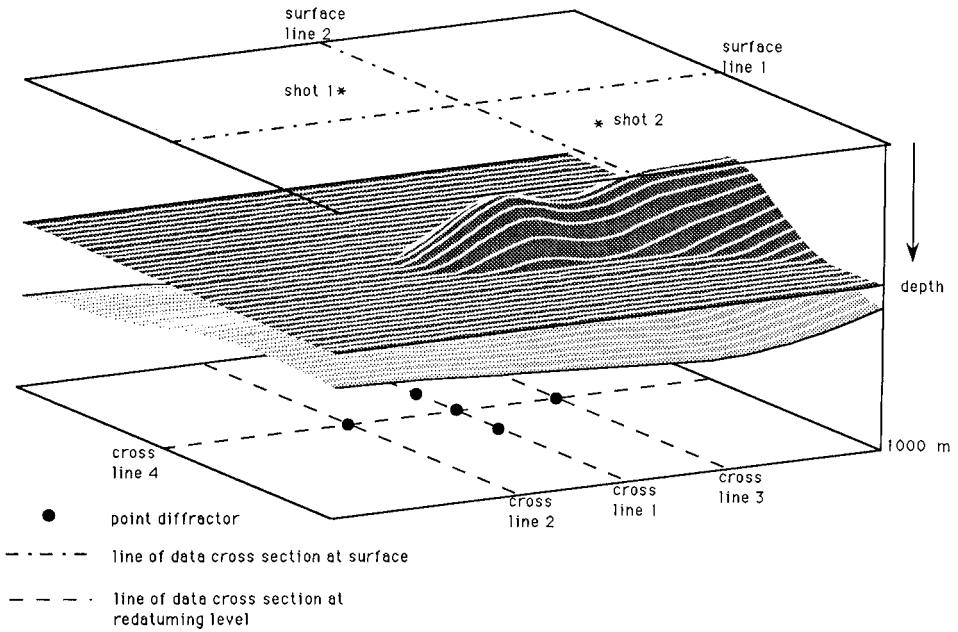


FIG. 19a. 3D subsurface model (perspective view).

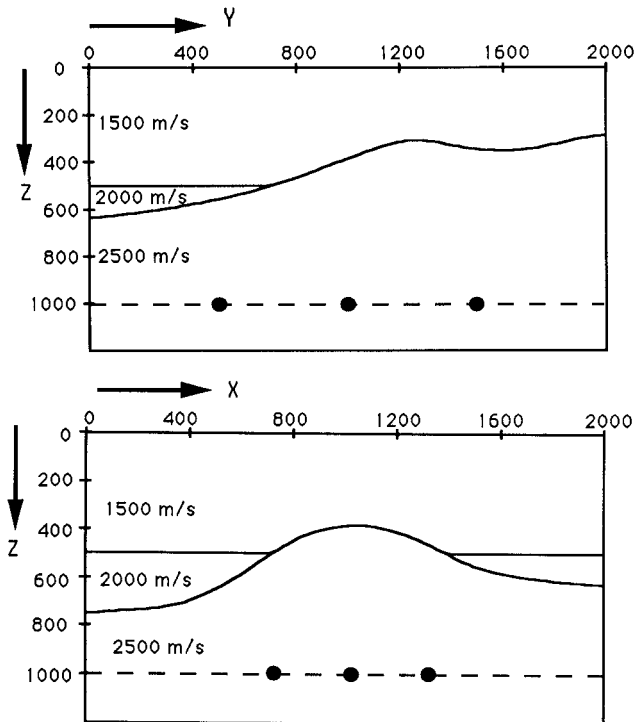


FIG. 19b. Two cross-sections through the 3D subsurface model.

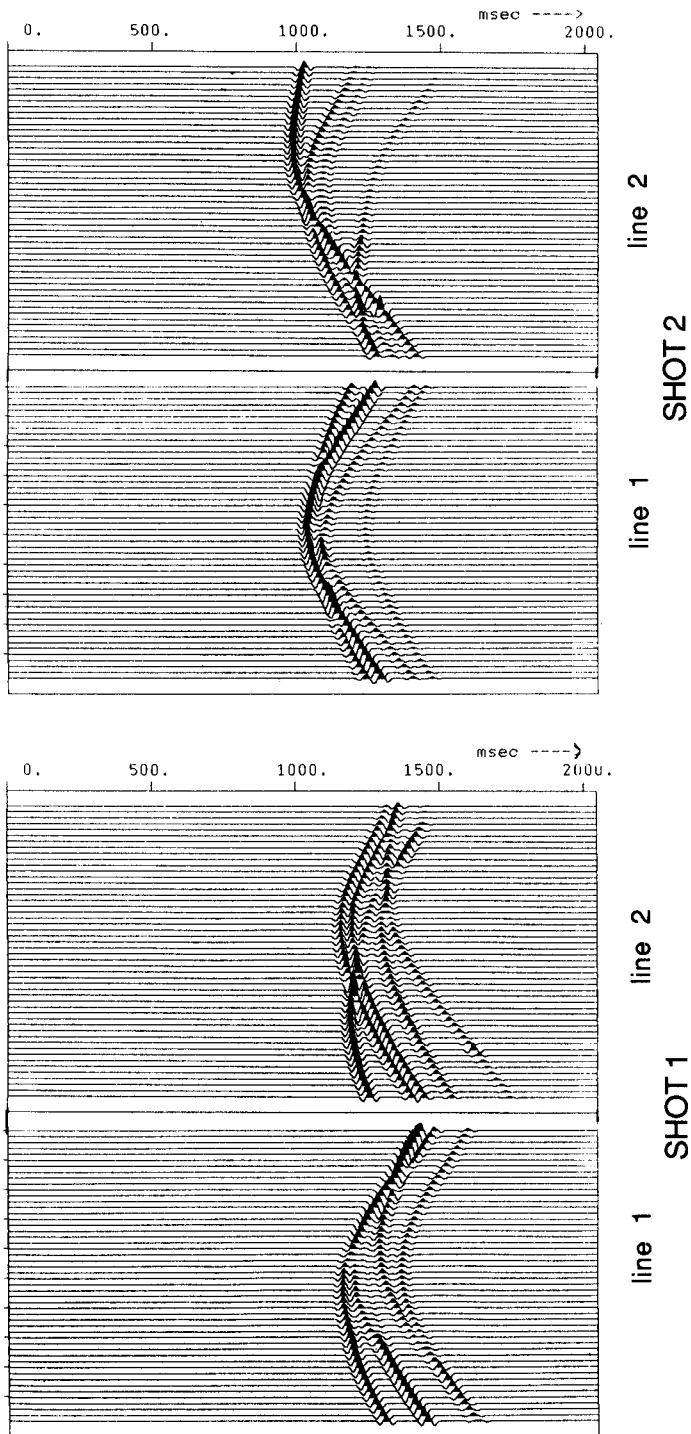
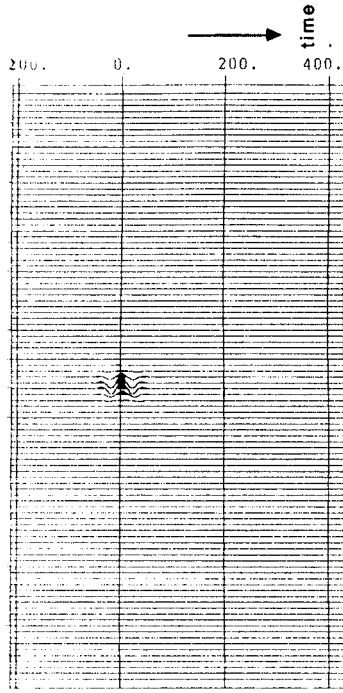
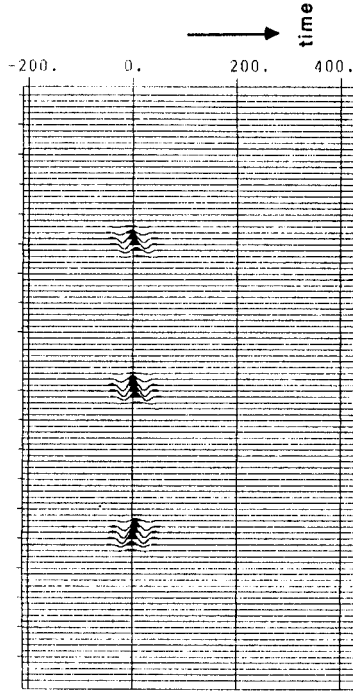


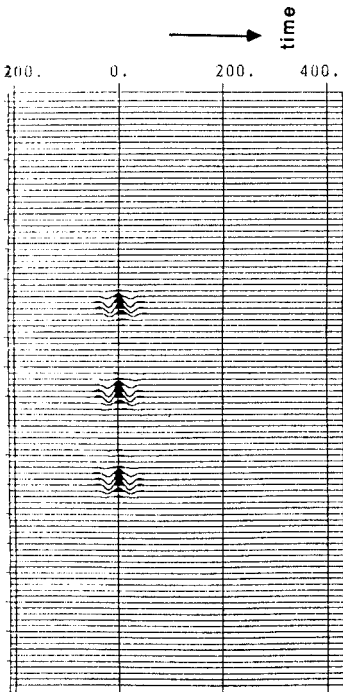
Fig. 19c. Cross-sections through two shot records, as indicated in Fig. 19a.



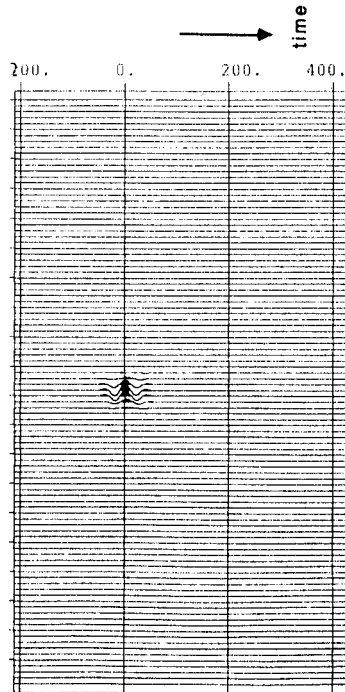
line 2



line 4



line 1



line 3

FIG. 19d. Four cross-sections through the result of 3D shot record redatuming to  $z = 1000$  m.

## ACKNOWLEDGEMENTS

We thank Marathon Oil Company for designing and creating the watertank model and data. Marathon does not necessarily endorse our processing procedures. The investigations were supported by the sponsors of the TRITON consortium project at the Laboratory of Seismics and Acoustics of the Delft University, The Netherlands.

## REFERENCES

- BERKHOUT, A.J. 1984. *Seismic Migration*, Volume B: *Practical Aspects*. Elsevier Science Publishing Co.
- BERKHOUT, A.J. 1985. *Seismic Migration*, Volume A: *Theoretical Aspects*, 3rd edn. Elsevier Science Publishing Co.
- BERKHOUT, A.J. and WAPENAAR, C.P.A. 1989. One-way versions of the Kirchhoff integral. *Geophysics* (in press).
- BERRYHILL, J.R. 1984. Wave equation datuming before stack. *Geophysics* **49**, 2064–2066.
- BERRYHILL, J.R. 1986. Submarine canyons velocity replacement by wave equation datuming before stack. *Geophysics* **51**, 1572–1579.
- BEYDOUN, W.B. and KEHO, T.H. 1987. The paraxial ray method. *Geophysics* **52**, 1639–1653.
- BLACQUIERE, G., DEBEYE, H.W.J., WAPENAAR, C.P.A. and BERKHOUT, A.J. 1989. Three-dimensional table driven migration. *Geophysical Prospecting* (submitted).
- CERVENY, V., POPOV, M.M. and PSENCIK, I. 1982. Computation of wave fields in inhomogeneous media – Gaussian beam approach. *Geophysical Journal of the Royal Astronomical Society* **70**, 109–128.
- COX, H.L.H., OOMS, F.P.J., WAPENAAR, C.P.A. and BERKHOUT, A.J. 1988. Verification of macro-subsurface models using a shot record approach. 58th SEG meeting, Anaheim, Expanded Abstracts, 904–908.
- DIX, C.H. 1955. Seismic velocities from surface measurements. *Geophysics* **20**, 68–86.
- HOLBERG, O. 1987. Computational aspects of the choice of operator and sampling interval for numerical differentiation in large-scale simulation of wave phenomena. *Geophysical Prospecting* **35**, 629–655.
- HUBRAL, P. 1976. Interval velocities from surface measurements in the three-dimensional plane layer case. *Geophysics* **41**, 233–242.
- JEANNOT, J.P. 1988. Full prestack versus shot record migration: practical aspects. 58th SEG meeting, Anaheim, Expanded Abstracts, 966–968.
- JEANNOT, J.P., FAYE, J.P. and DENELLE, E. 1986. Prestack migration velocities from depth focussing analysis. 56th SEG meeting, Houston, Expanded Abstracts, 438–440.
- KEHO, T.H. and BEYDOUN, W.B. 1988. Paraxial ray Kirchhoff migration. *Geophysics* **53**, 1540–1546.
- PEELS, G.L. 1988. True amplitude wavefield extrapolation with applications in seismic shot record redatuming. Ph.D. thesis, Delft University of Technology.
- POSTMA, R.W. and JEANNOT, J.P. 1988. Prestack depth imaging beneath complex overburden. 58th SEG meeting, Anaheim, Expanded Abstracts, 596–598.
- SCHULTZ, P.S. and SHERWOOD, J.W.C. 1980. Depth migration before stack. *Geophysics* **45**, 361–375.
- TRITON, 1985. Target oriented 3D migration. Consortium proposal, Delft University of Technology.
- VAN DER MADE, P.M. 1988. Determination of macro-subsurface models by generalized inversion. Ph.D. thesis, Delft University of Technology.

- VERSCHUUR, D.J., HERRMANN, P., KINNEGING, N.A., WAPENAAR, C.P.A. and BERKHOUT, A.J. 1988. Elimination of surface-related multiply reflected and converted waves. 58th SEG meeting, Anaheim, Expanded Abstracts, 1017–1020.
- WAPENAAR, C.P.A. and BERKHOUT, A.J. 1987. Full prestack versus shot record migration. 57th SEG meeting, New Orleans, Expanded Abstracts, 761–764.
- WAPENAAR, C.P.A., PEELS, G.L., BUDEJICKY, V. and BERKHOUT, A.J. 1989. Inverse extrapolation of primary seismic waves. *Geophysics* (in press).
- YILMAZ, O. and LUCAS, D. 1986. Prestack layer replacement. *Geophysics* **51**, 1355–1369.